Geomechanics for Energy and the Environment 45 (2026) 100797

Contents lists available at ScienceDirect

Geomechanics for Energy and the Environment

journal homepage: www.elsevier.com/locate/gete

Mechanisms of induced seismicity due to geothermal operations in the Dinantian fractured carbonates in Mol, Belgium

Brecht B.T. Wassing [a,*], Justin Pogacnik [b], Matsen Broothaers [b], Loes Buijze [a], Johannes H.P. de Bresser [c]

[a] TNO-Geological Survey of the Netherlands, Princetonlaan 6, Utrecht 3584 CB, the Netherlands
[b] VITO, Boeretang 200, Mol 2400, Belgium
[c] Faculty of Earth Science, Utrecht University, Utrecht 3508 TA, the Netherlands

ARTICLE INFO

Keywords:
Induced seismicity
Fault reactivation
Aseismic slip
Thermohydromechanical
Modelling, geothermal

ABSTRACT

The geothermal project at the VITO Sustainability Park in Mol targets the fractured carbonates of the Dinantian formation. During balanced geothermal operations, several earthquakes were recorded, with a maximum magnitude of M_L 2.2. To better understand the mechanisms driving this seismicity, we developed a thermo-hydro-mechanical model to simulate pressure, temperature and stress changes on a fault near the injection well, which hosts most of the seismic events. Given the observations of a low stress drop and low seismic moment release, the fault is represented in the model as comprising a few isolated asperities embedded within a broader aseismic zone. Although the model geometry is simplified, and both flow and mechanical behavior are not fully constrained, it shows potential to reproduce the main characteristics of field observations of seismicity at the geothermal site. Our simulations indicate that thermal effects had limited influence on fault stress, primarily due to the relatively small injected volumes. Rate effects - through rapid poroelastic unloading immediately after shut-in – may have facilitated seismogenic slip after shut-in. Aseismic slip, primarily driven by pressure increases, appears to have played a significant role in fault reactivation. The model results suggest that stress transfer from aseismic slip to fault asperities may have been a key driver of seismicity, particularly for larger events occurring at greater depths and farther from the injection well.

1. Introduction

Ambitions to accelerate geothermal energy production require the development of new geothermal targets. One such a target in north-western Europe is the Dinantian fractured carbonates play.[1] The VITO geothermal project on the site of former Balmatt Industries in Mol is the first deep geothermal project in the fractured carbonates of the Dinantian Carboniferous Limestone Group that was realized in northern Belgium.[2–5] The site consists of a geothermal plant with three wells (Fig. 1). The geothermal site is operated under balanced conditions, with fluid injection rates closely matching production rates to minimize pressure changes in the reservoir. During short cycles of balanced circulation between December 2018 and June 2019, several earthquakes were recorded, with a maximum M_L 2.2 seismic event on June 23rd, 2019. The event led to suspension of geothermal activities.[5,6] Operations were resumed in April 2021, and the site was operated as a research facility until the occurrence of a M_L 2.1 seismic event on November 16th 2022, which prompted a hold to all activities at the site. Both the M_L 2.2 and M_L 2.1 seismic events were felt by the population in the nearby cities of Dessel and Mol, with some damage reported following the M_L 2.1 earthquake (pers.comm. VITO). This paper covers the period and dataset from December 2018 to December 2022.

Given the proximity of the geothermal site to the towns of Dessel and Mol, as well as the nuclear facilities in Dessel and Mol, a reliable assessment of seismic hazard and effective management of seismic risk are essential. A robust mechanistic understanding of the interplay between geothermal operations, fault reactivation and induced seismicity at the geothermal site is critical for assessing and managing these risks.

In balanced geothermal systems like the one in Mol, pressure changes due to fluid production and injection, as well as cooling from the injection of cold water, lead to stress changes in the reservoir, involving multiple mechanisms that can cause fault reactivation and induced seismicity. Numerous studies have investigated the causes of induced earthquakes during geothermal operations in fractured or faulted rocks,

* Corresponding author.
E-mail address: brecht.wassing@tno.nl (B.B.T. Wassing).

https://doi.org/10.1016/j.gete.2026.100797
Received 9 September 2025; Received in revised form 21 January 2026; Accepted 29 January 2026
Available online 31 January 2026

such as those present at the geothermal site in Mol. A comprehensive overview by Buijze et al.[1] outlines key mechanisms driving stress changes and induced seismicity in fractured geothermal reservoirs, including pore pressure diffusion, poroelasticity, thermoelasticity, stress transfer and chemical alteration of faulted rocks. Boyet et al.[8] demonstrate that poroelastic stressing can extend beyond the zone of pressure diffusion and has likely contributed to post-injection fault reactivation in the Basel Enhanced Geothermal System, particularly in distant faults. Vörös and Baisch[9] address the interplay between long-term thermoelastic stressing and a rapid pore pressure increase, proposing it as the root cause behind seismic activity in Dinantian fractured carbonates in the southern Netherlands. Hager et al.[10] found that most seismicity near an injection well in the fractured carbonate reservoir of the Val 'd'Agri field in Italy was associated with Coulomb stress values exceeding previous maxima, but explain the occurrence of seismicity at lower Coulomb stress values using a rate-and-state seismicity model. Several other studies[11–17] discuss the interaction between fluid diffusion and aseismic slip, where fluid pressure buildup in faults initiates aseismic slip that, in turn, transfers stresses to earthquake-prone asperities. This aseismic stress transfer can affect fault segments at much larger distances from the injection well than the pressure front. Kinscher et al.[6] suggest that aseismic creep may have played an important role in driving seismicity at the geothermal site in Mol.

These studies indicate that multiple mechanisms can drive seismicity in fractured media, and that the dominant mechanism is dependent upon site-specific geological and operational conditions. A comprehensive quantitative assessment of the distinct contributions of different physical mechanisms driving seismicity at the geothermal site in Mol is still lacking. This gap limits the possibility to accurately assess seismic hazards and implement effective mitigation strategies.

The objective of this study is to improve our understanding of the mechanisms driving induced seismicity in the fractured rocks at the site in Mol. To achieve this, we employ a coupled thermo-hydro-mechanical model and analyze the effects of geothermal operations on pressure and temperature changes, fault loading and seismicity. Specifically, we investigate the roles of pressure diffusion, poroelasticity, thermoelasticity and aseismic slip. We validate our models by comparing simulated outcomes with the main characteristics of observed seismic activity. Beyond providing site-specific insights, the findings can contribute to understanding fault reactivation and seismic hazard assessment and they can enable the future development of effective risk mitigation strategies for other geothermal activities within the Dinantian carbonates.

2. Geology, operations and seismicity at the Mol geothermal site

2.1. Litho-stratigraphical sequence

The wells target the fractured carbonates of the Carboniferous Limestone Group, also known as Dinantian carbonates.[2] The lithostratigraphical succession is shown in Fig. 2, based on information from Mol-GT-03, which was drilled through the entire carbonate sequence. The Carboniferous Limestone Group, consisting of limestones, dolomites and claystones, is found between a depth of around 3150 m and 3990 m below the surface. On top of the Dinantian carbonates lie shales and claystones (Souvré Formation) which form the transition to the Upper Carboniferous coal bearing formations. At the base, claystones, shales and carbonates of the Pont d'Arcole and Bosscheveld Formation form the transition to Upper Devonian sandstones with interbedded claystones (Evieux Formation (Condroz Group)).[2]

2.2. Structural geological setting and in-situ stresses

At the time of drilling, three major (N)NW – (S)SE striking regionally mapped normal fault structures were interpreted from 2D seismics to intersect the Dinantian carbonates at and close to the geothermal site (Fig. 2). Notably, the production well Mol-GT-01 was drilled into the fault zone of one of these regional faults, whereas the injection well Mol-GT-02 targeted a reservoir section that was, at the time, assumed to be located between two of the mapped faults. Based on an additional seismic line, reprocessing of the 2D seismic data and the spatial distribution of seismic events, the conceptual structural model was later

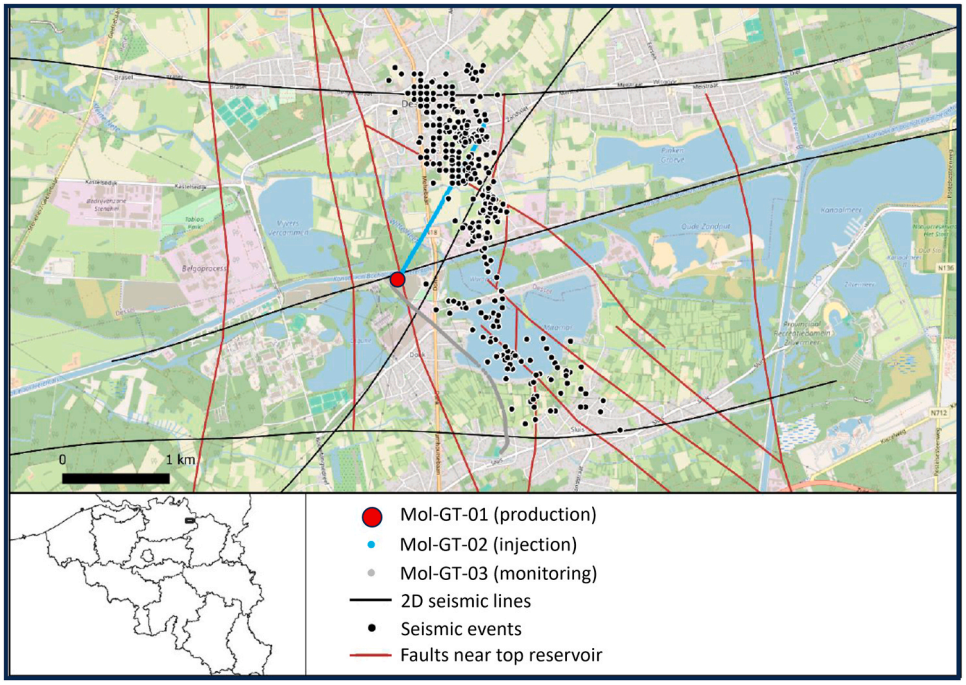

Fig. 1. Map view with the location of the geothemal site, well trajectories, seismic lines, seismic event locations and fault traces at the top of the Dinantian carbonate reservoir.
Adapted from: Pogacnik.[7]

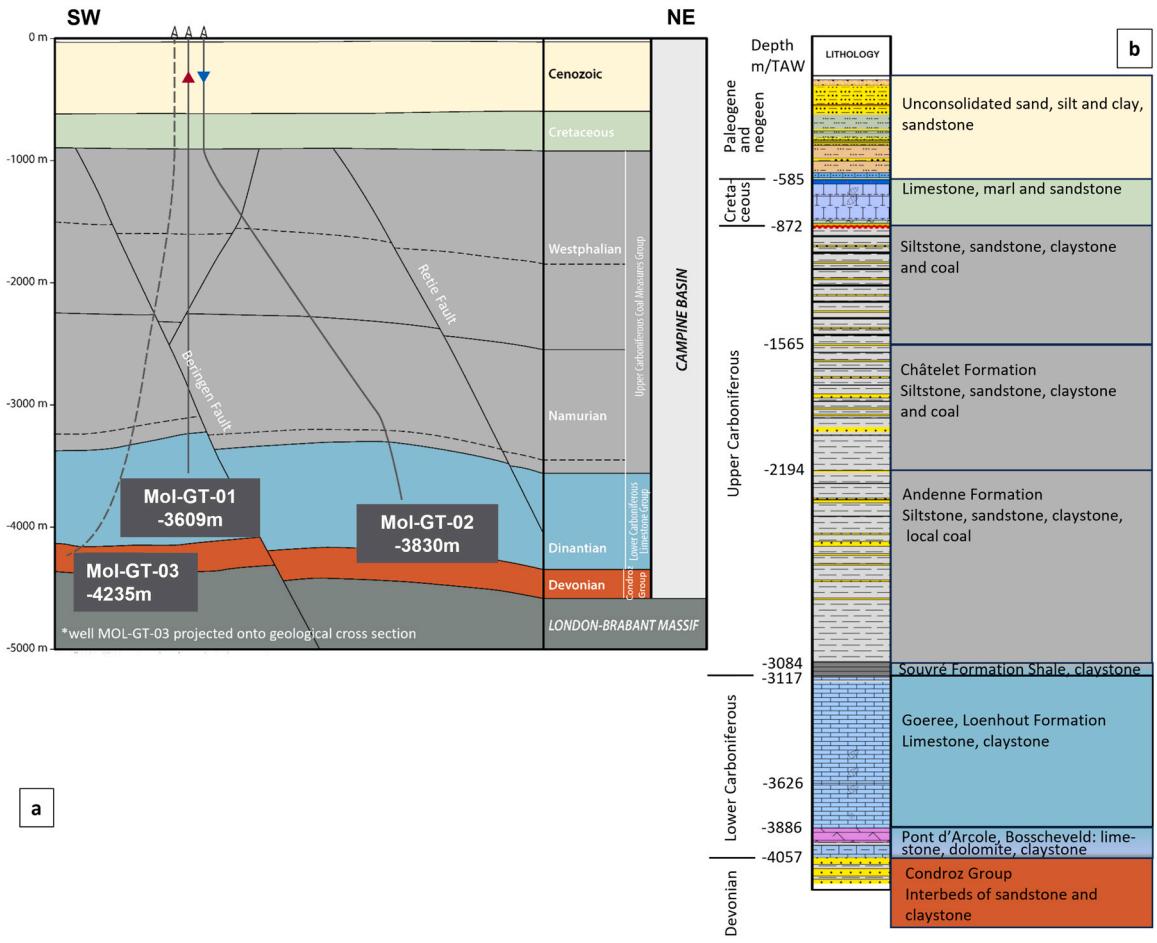

Fig. 2. a) Schematic overview of main regional faults at the Mol-Dessel area and well trajectories of the geothermal project, (horizontal distances not to scale and details of local fault structures re-interpreted from 2D-seismics are not included in this figure), b) lithostratigraphy interpretation of Mol-GT-03.

reinterpreted as shown in Fig. 1. In addition to the regional fault set, a series of steeply dipping WNW–ESE to NW–SE striking fault segments intersect the Dinantian carbonate reservoir. Furthermore, a set of steep, en echelon fault segments aligned N–S to NNW-SSE has also been interpreted, which cross-cuts the upper part of the Dinantian carbonates.[4] The injection well is located west of, and in close proximity to this approximately NNW-SSE striking fault structure, and just north of a WNW–ESE striking fault (see Fig. 1).

In-situ stress directions derived from image logs (i.e. borehole breakouts and drilling induced fractures) indicate a maximum horizontal stress direction of N330° – N350°, which is consistent with the regional directions reported for this area.[18,19] In-situ stress measurements, to derive magnitudes of the in-situ stress components, are not available for the Mol geothermal site. Focal mechanisms of the induced seismic events reported at the site are predominantly strike slip, and indicate overall strike-slip faulting on either NNE-SSW or WNW-ESE to WE striking faults,[6] see also Section 2.3.

2.3. Operations and seismicity

Phase I December 2018 – June 2019. Seismicity was first detected by the national network during the initial testing phase of the well and led to the installation of a local seismic monitoring network, consisting of a six-station borehole network, with sensors between 30 and 600 m depth, with a magnitude of completeness of Mc = 0.6.[6] A total of 285 seismic events were automatically detected from soon after the start-up of operations until October 2019 (Fig. 3). Seismicity occurred mainly during injection or at shut-in of the well.[6] A M_L 2.2 event was recorded on June 23rd 2019, two-and-a-half days after an unplanned power-cut. The event was preceded by a significant increase in seismicity rate before the power-cut. The focal mechanisms indicate predominant strike-slip movement, i.e. either right-lateral strike slip movement on approximately E-W to WNW-ESE oriented fault planes, or left-lateral strike-slip movement on approximately N-S oriented fault planes.[6] Kinscher et al.[6] reported that seismicity was located at reservoir depth (3500–4000 m), several hundred meters to the West of the injection well and show that seismicity appeared in eight dense spatial clusters (isolated 'families' of events). The largest event of M_L 2.2 has been located at a depth of around -3700m. Relative locations of seismic events highlight sub-vertical structures, while the alignment of relative event locations in an almost E-W direction points to this being the most active fault orientation,[6,7] see also Fig. 4. The inferred stress drops are in the range of 0.1–10 MPa.[6] The majority of the clustered events show strongly similar wave forms which are generally interpreted to be caused by a repeated rupture of a single asperity (seismic repeater) or by ruptures of closely neighbouring asperities with the same source mechanisms (seismic multiplet).[6]

Phase II April 2021 – November 2022. Operations were resumed in April 2021, albeit at lower rates than in Phase I. Prior to the restart of injection activities, the seismic monitoring network was upgraded to a 16-station array, including sensors installed at the surface and at depths between 30 and 600 m. For this network, the magnitude of completeness is estimated at Mc ~-0.4. In addition, a deep borehole sensor was installed at a depth of 2052 m, reducing the magnitude of completeness to Mc ~-2.0.[20]

From November 2021 to December 2022, 232 seismic events were

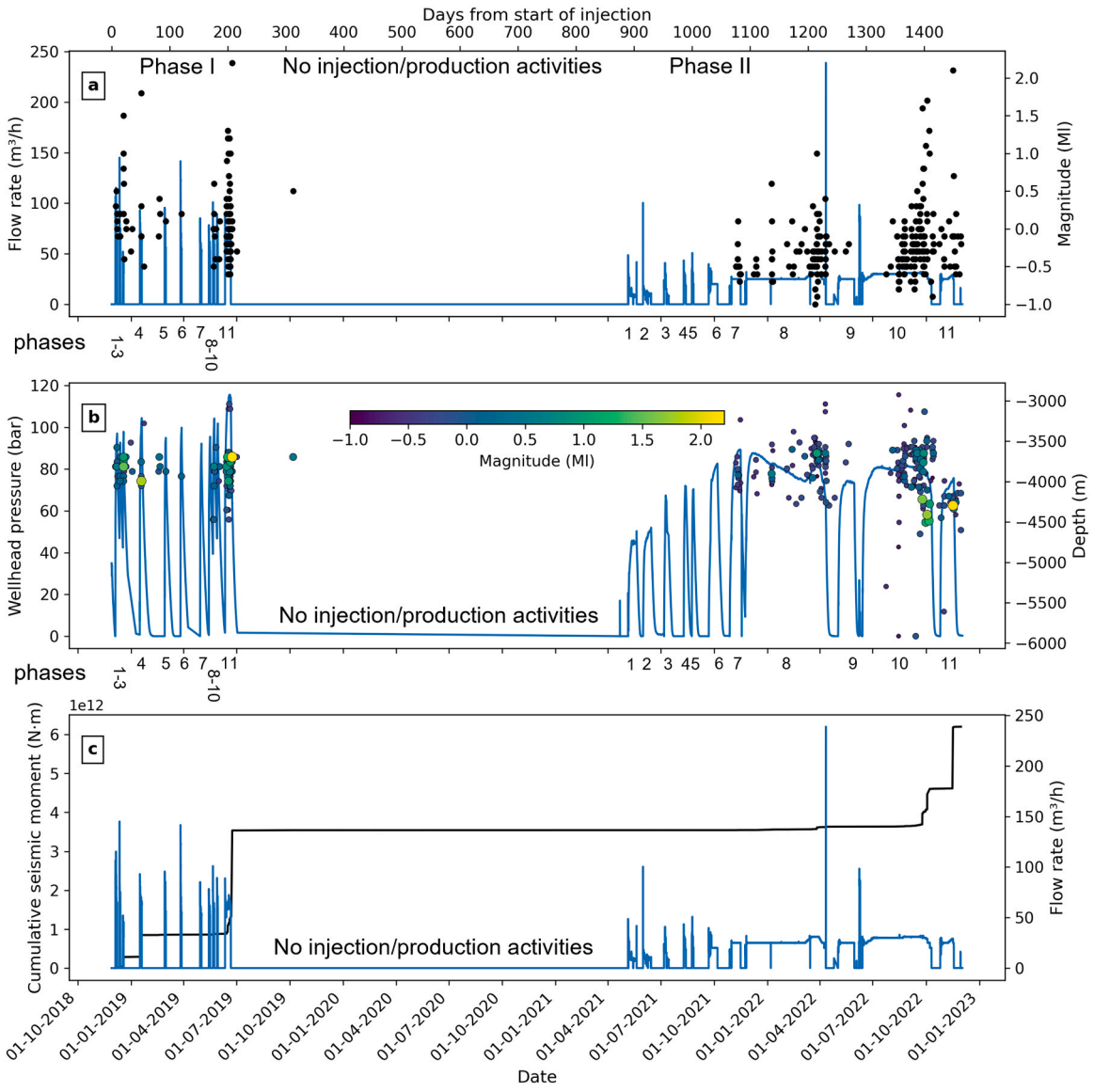

Fig. 3. Temporal evolution of operations and observed seismicity at the Mol geothermal site. a) flow rates (blue line) and magnitudes of seismic events (dots), b) wellhead pressures (blue line), magnitudes (colored dots) and depths of seismic events, c) cumulative seismic moment release (black line, based on M_L and automatically detected events) and flow rate (blue line). Note that in this figure only seismic events automatically detected by the 16-station microseismic monitoring network are plotted; it does not include events recorded only by the deep borehole sensor.

recorded. It is worth noting that the temporal and spatial distributions of seismicity shown in Figs. 3 and 4 for Phase II are based exclusively on seismic events automatically detected by the 16-station microseismic monitoring network and that they neither include events recorded only by the deep borehole sensor, nor events derived from template matching. A detailed analysis of the complete microseismic catalogue derived (>10000 events) is provided by Gautam et al.[20,21] We note that this dataset was not publicly available at the time of writing.

Fig. 4 indicates a restart of seismicity in phase II.7 in November 2021[5] (for phase definitions, see Fig. 3), based on events recorded by the 16-station seismic network, at lower rates and well-head pressures than in phase I. Based on microseismicity detected by the deep borehole station, Gautam et al. [20,21] report an earlier restart of seismic activity, with first microseismic events occurring shortly after shut-in at the end of phase II.2, followed by some isolated events during phases II.3 and II.4, and a subsequent increase in activity during phase II.6. Seismicity rates and magnitudes pick up considerably during the two prolonged injection periods of phase II.8 and II.10 (Fig. 3a and b). Gautam et al.[20] report a b-value derived from the deep borehole catalogue of 0.9 (± 0.01), which is lower than obtained from the 16-station catalogue (1.2 ± 0.1). This is due to undersampling of smaller-magnitude events in the surface network.[20] More specifically, they report an increase in event rate at an injection flow rate of ~31 $m^3\ h^{-1}$ in the second half of phase II.8, accompanied by a marked decrease in b-value and an increase in seismic efficiency, which they interpret as a change in mechanism driving fault reactivation.[20,21]

Overall, the location of seismic events near the injection well defines a NNW-SSE elongated area, aligned with the N-S to NNW-SSE structure in Fig. 1. The event locations in Phase II are shifted slightly towards the Southeast compared to those in Phase I in 2018–2019 (Fig. 4a). This may be partly due to a network bias, as the network in 2021–2022 comprised several additional stations around the epicentral area. At the time of writing this paper, a detailed comparison between the event locations was still ongoing. Seismicity migrates southward during progressive injection in Phase II, reaching almost 3 km South from the injection point (Fig. 4a). The southern cluster of seismic events highlights a number of NW-SE oriented structures. The location uncertainty of the events in the South is higher, because of the more sparse network

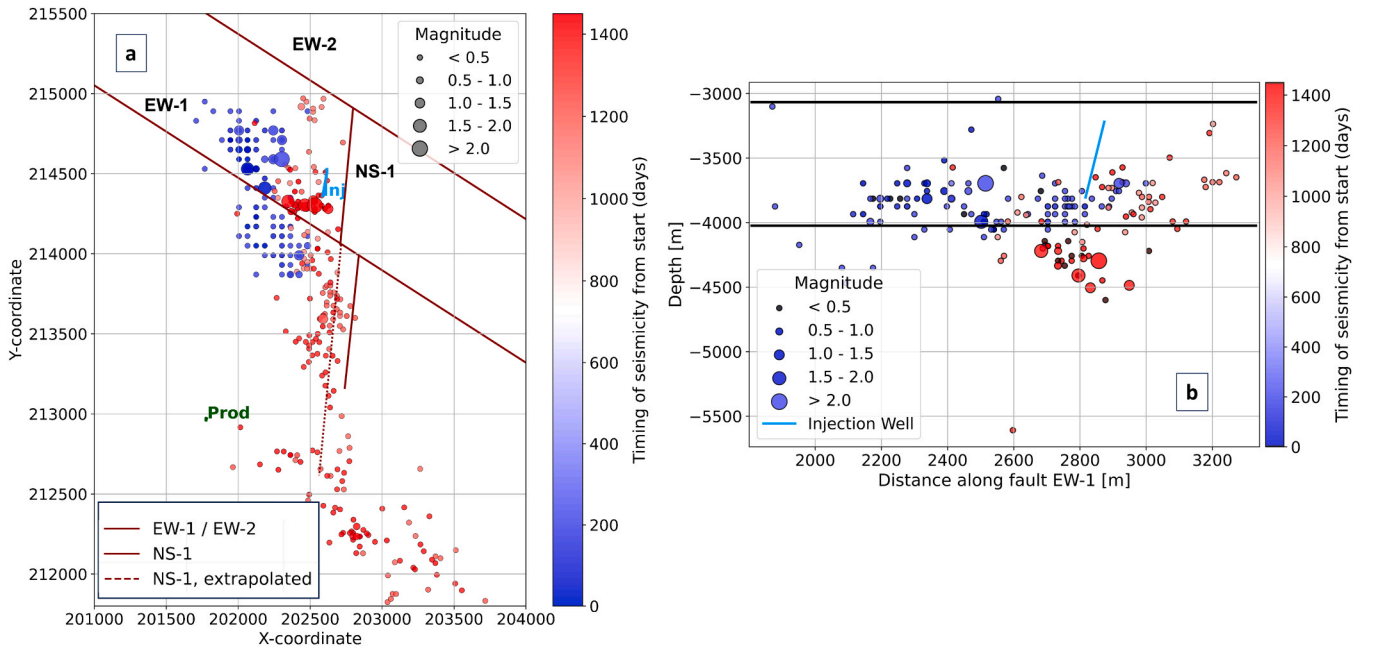

Fig. 4. Timing and locations of seismic events, a) lateral position with all events (phase I and II, 2018–2022), with zoom in on locations of faults EW-1, EW-2 and NS-1 included in the model; in the model NS-1 is extrapolated southward – the trailing segment is not explicitly modelled; b) vertical cross section along the strike of fault EW-1, with seismic events within 300 m distance from fault EW-1 - and projected on fault EW-1, phase I and II. Solid black lines present top and bottom of the Dinantian carbonates. Note that in this figure only seismic events automatically detected by the 16-station microseismic monitoring network are plotted; it does not include events recorded only by the deep borehole sensor.

coverage. Another observation is the reactivation of deeper segments of the NW-SE fault located directly South of the injection well after a prolonged period of injection (cycle II.10 in Fig. 3b, and Fig. 4b). Mean hypocenter locations of all but one of the seven events with magnitudes M_L 1.0 and larger are located below a depth of 4000 m, around the Carboniferous-Devonian transition. The M_L 2.1 event has been located at a depth of -4296m.

3. THM-simulation in TOUGH2-FLAC3D

3.1. Modelling approach

We use a coupled THM (thermo-hydro-mechanical) numerical model to analyse the effect of pressure and temperature variations on fault stability and induced seismicity. Our approach involves an iterative coupling of TOUGH2 and FLAC3D, based on adaptation of the code originally described in Taron and Elsworth.[22] At each time step, the flow-simulator TOUGH2 computes fluid pressure and temperature, and these are subsequently used in FLAC3D to compute displacements, stresses and strains. Stresses computed in FLAC3D are used to update pressures before the next computation step in TOUGH2 is performed. TOUGH-FLAC allows for advanced modeling approaches, such as simulation of double porosity/permeability systems and stress-dependent fracture opening and related permeability and porosity changes. However, these are computationally demanding, particularly in 3D, and heavily reliant on detailed input data, and for the case of the geothermal project in Mol, many of the key flow- and mechanical parameters of the fractured Dinantian carbonates and underlying Devonian sandstones are unknown. Therefore, instead of adopting a fully coupled THM modeling approach for a fractured medium, we represent the reservoir using a single-porosity framework, explicitly incorporating fractures and fault zones as discrete geometries with finite thicknesses. This way we capture the dominant flow behavior associated with these structures while remaining consistent with the level of data available.

3.2. Model geometry

Fig. 5 shows the simplified geometry of the THM model. The size of the mechanical model in FLAC3D is 5.1 km x 5.1 km x 2.5 km and includes the lithostratigraphical units between -2500 m and – 5000 m depth. The reservoir model in TOUGH2 covers a subsection of the mechanical model and only includes the low permeability claystones and shales of the Souvré Formation, the reservoir rocks of the Lower Carboniferous Limestone Group and part of the underlying Devonian. We incorporate only the three faults closest to the injection well in our geomechanical model (Fig. 1 and Fig. 4a). The fault geometry and orientation is based on the geological interpretation in Fig. 1 and the relative hypocenter locations and focal mechanisms of microseismicity. Focus of the analysis is on the reactivation of fault EW-1 to the South of the injection well, that likely hosts the larger seismic events.

3.3. Model parametrisation and boundary conditions – (heat)flow

The estimates of the flow parameters (layers, porosity, permeability) are based on the analysis of well tests and reservoir behaviour by the geothermal operator, and the description of the reservoir model for the Mol geothermal site.[7] We model the Dinantian reservoir as an 800 m thick horizontal unit throughout the entire model, without considering the generally low dip of the reservoir and the reservoir offset of layers caused by faults. In our model, we assume that fault damage zones significantly contribute to the flow in the reservoir. In addition, based on loss zones and flow measurements in Mol-GT-01 and Mol-GT-02, we assume that two 50 m thick intervals in the upper part of the reservoir significantly contribute to flow[7] and assign a higher permeability to these layers (res1 and res3 in Table 1 and Fig. 5). The NNW-SSE fault structure (NS-1) located 150 m to the east of the injection well is interpreted to form a high-permeability pathway along which seismicity spreads southwards in time. The WNW-ESE fault zones (fault EW-1 and EW-2) are located some 300 and 500 m to respectively the south and north of the injection well. They are assigned a high along-fault permeability and a lower permeability across-fault; fault EW-1 acts as

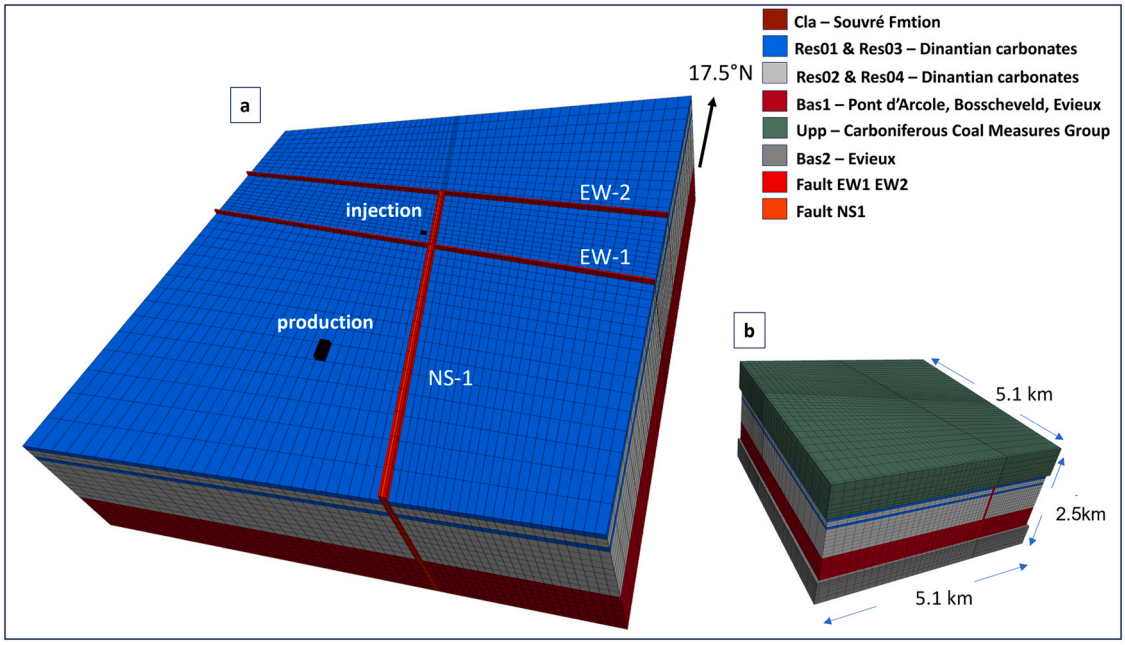

Fig. 5. a) Geometry, layers and faults in the reservoir model (TOUGH2), including the locations of injection and production well. In red: High permeability N-S oriented flow path (NS-1) and two E-W faults (EW-1 and EW-2). Blue layers are high permeability layers in the top of the reservoir (res1 and res3), light gray layers are low permeability matrix rocks in the Dinantian carbonates (res2); brown layer is the transition to and top of the Devonian below the carbonate reservoir (bas1). Top clay layer (cla) not shown. b) Geometry of the FLAC3D – mesh, including over-and underburden layers (bas2 and upp). For layer parameters, see Table 1. Note that an anti-clockwise rotation of 17.5 ° was used to optimize the numerical mesh with regard to the orientation of the faults.

Table 1
Hydrological and geomechanical parameters. ρ: density, E: Young's modulus, ν: Poisson's ratio, k: permeability, n: porosity, α: Biot coefficient, α_T: thermal expansion coefficient, k_t: thermal conductivity, c_p: specific heat, $\mu_{aseismic}$: static friction coefficient for aseismic fault, $\mu_{asperity}$: static friction coefficient for asperity, C_0: initial cohesion.

Model units	ρ (kg/m3)	E (MPa)	ν (-)	k (m^2)	n (-)	α (-)	α_T (/°C)	k_t (W/m°C)	c_p (J/kg°C)
Upp	2740[7]	40[5]	0.28						
Cla	2740[7]	40[5]	0.28	1e-17	0.005	1	1e-5	1.2	900
Res1	2740[7]	40[1,2,3]	0.28[1,2]	1e-15[4]	0.01[4]	0.6[1]	1e-5	2.6	900
Res2				5e-16	0.02				
Res3				1e-15	0.01				
Res4				1e-16	0.02				
Bas1	2740[7]	40[5]	0.28	1e-17	0.005[4]	1	1e-5	2.6	900
Bas2	2740[7]	40[5]	0.28						
NS-1	2740[7]	40[5]	0.28	1e-14 (//) 1e-15 (⊥)	0.05[4]	0.6	1e-5	2.6	900
EW-1, EW-2	2740[7]	40[5]	0.28	2e-15 (//) 1e-16 (⊥)	0.025[4]	0.6	1e-5	2.6	900
	$\mu_{aseismic}$ (-)	**$\mu_{asperity}$ (-)**	**C_0 (MPa)**	**Ψ**					
EW-1	0.63[6]	0.65[6]	0.0	0					
In-situ stress	**S_v (MPa)**	**S_{Hmax} (MPa)**	**S_{hmin} (MPa)**						
3800 m depth	91	91	54						

[1]) Goense,[23] [2]) pers.comm. Kane, [3]) Soustelle et al.,[24] [4]) based on well logs and well testing, no information available on permeability in the Devonian formations, but it is expected to be low and fracture-dominated, // along-fault flow permeability, ⊥ across-fault permeability, [5]) no information on the elastic properties of the over- and underlying formations was available; values for Young's modulus and Poisson's ratio similar to Dinantian carbonate values, [6]) for carbonates: Kane et al.,[25] [7]) from density logs – average value for interval 2500–5000 m.

a baffle to southward flow in the fault and fracture zone NS-1.[7] Fault damage zone width is assumed to be 20 m and 10 m for fault NS-1 and EW-1, EW-2 respectively. All faults in the model are vertical and are present in the caprock, reservoir and upper part of the underburden, see also Fig. 5, though in the current interpretation faults are assumed to be only permeable within the reservoir section. Model input parameters are given in Table 1.

Pressure and temperature evolution in the reservoir has been modelled in TOUGH2, using a temperature-dependent viscosity and density for the fluid. Horizontal pressure boundary conditions have been applied to the TOUGH2 mesh, with no-flow boundary conditions set at the top and bottom. Additionally, heat transfer at the top and bottom boundaries is assumed negligible, and temperatures are fixed on the sides. A hydrostatic pressure is used to obtain the initial pressure field; reservoir temperature is assumed to be a constant 140°C. The wells have not been explicitly modelled; fluid injection is modeled directly into the mesh elements of the Dinantian reservoir at the well locations. For both phases 11 injection/production cycles have been modelled. Actual flow

data from previous operations (Fig. 4a) are used to derive an average constant injection rate for each cycle, additionally including the gradual increase in flow rate after 1200 days, at the end of phase II.8. An average injection temperature of 65°C is used based on injection temperature data.

3.4. Model parametrisation and boundary conditions - geomechanics

Roller boundary conditions are applied to the vertical and bottom boundary of the model. Initial stress conditions are based on well data, where caliper and borehole FMI logs indicate a consistent maximum horizontal stress (S_{Hmax}) orientation of 158°N.[6] The total vertical stress (S_v) is derived from well density logs. However, the magnitudes of horizontal in-situ stresses (S_{hmin} and S_{Hmax}) in the Dinantian carbonates and Devonian units are poorly constrained. Focal mechanisms from induced seismicity indicate a (transtensional) strike-slip regime, with $S_{Hmax} > S_v > S_{hmin}$.[6] To reflect this regime, we apply a S_{Hmax} that is close to S_v and significant anisotropy between S_{Hmax} and S_{hmin}. Horizontal stress gradients are chosen such that stress conditions on the WNW–ESE-oriented faults within the reservoir are near-critical, which aligns with the observed onset of seismicity shortly after injection operations began. Stress magnitudes are provided in Table 1.

All rock lithologies are modelled as isotropic, elastic materials, with geomechanical parameters summarized in Table 1. No core material is available from the Mol site, so elastic parameters (Young's modulus, Poisson's ratio, Biot coefficient) and strength parameters (cohesion and friction coefficient) are based on experimental results from analogue samples of the Dinantian carbonates[23,25] and Kane (pers. comm., 2024). Young's modulus was also obtained from sonic logs, using empirical relations to convert dynamic to static values,[24] and density was derived from density logs. Mechanical properties of the Devonian sandstones and overlying units are assumed to be similar to those of the Dinantian carbonates.

As seismic events in the northern part of the seismic cloud show predominantly strike-slip on structures that are oriented E-W to WNW-ESE, we analyse stress changes on fault EW-1. Fault EW-1 is represented by a discrete interface that can be assigned a Mohr–Coulomb failure criterion to simulate fault slip and to assess the contribution of aseismic fault slip to fault loading and fault reactivation.[15,26] The shear strength of the interface is defined by:

$$\tau_{max} = C_0 + \mu\sigma'_n \quad (1)$$

where μ is static friction coefficient, C_0 is cohesion, τ_{max} is shear strength and σ'_n effective normal stress. No frictional weakening is implemented, so if shear strength is exceeded, the fault slips 'aseismically' without a stress drop.

We introduce five localized strong asperities on fault EW-1 at different depths and distances from the injection well (Fig. 6c for locations). In nature, such asperities could arise from e.g. jogs or kinks on the fault plane or other heterogeneities, here modeled in a simplified manner as elastic inclusions. Notably, asperities are modelled as elastic, but a friction coefficient of 0.65 is used for the asperities in the computation of the Coulomb stress calculations, see Section 4; this higher friction coefficient represents the higher strength of the asperities as compared to the surrounding fault surface. The surrounding fault

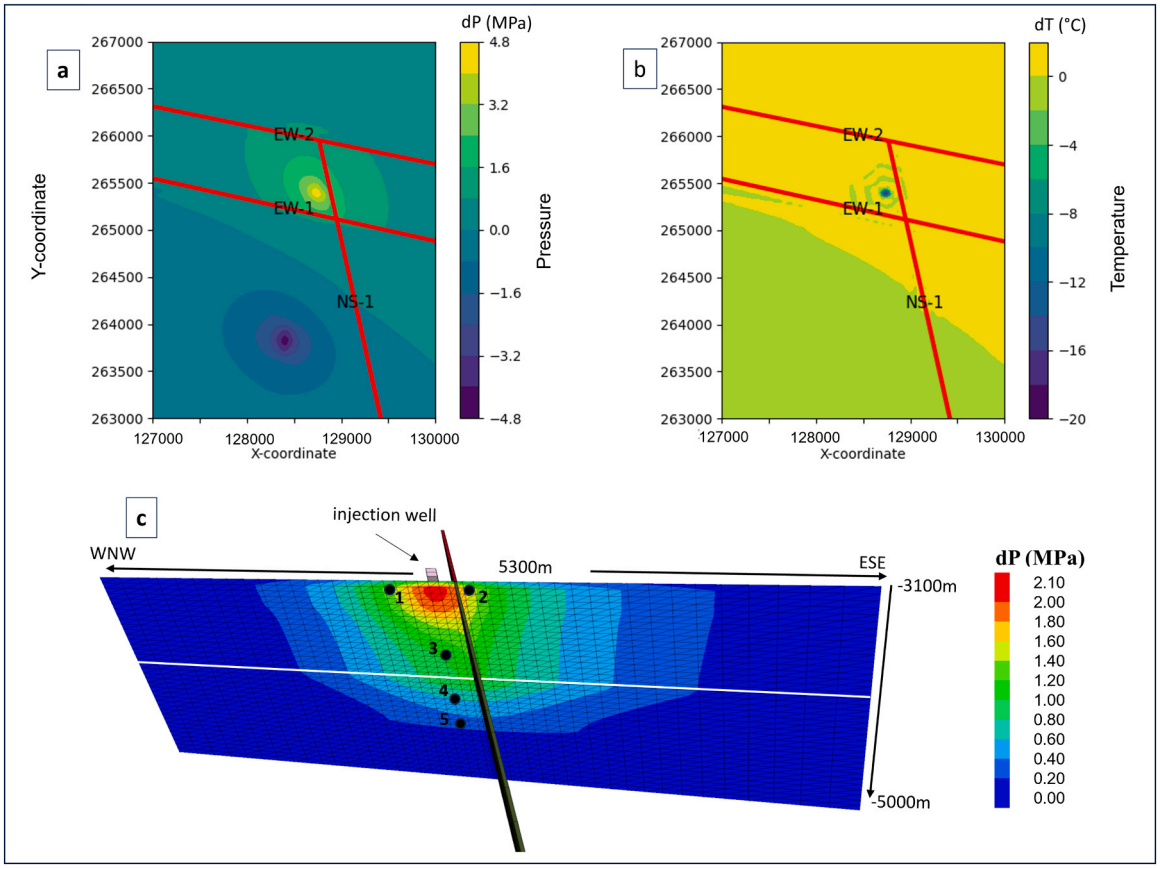

Fig. 6. a) Map view of a) pressure change and b) temperature change in the reservoir at a depth of ~3300 m below surface level at the time of the M 2.1 event, end of phase II. Red lines represent faults. c) Pressure change on the fault EW-1 at the time of the M 2.1 event, end of phase II. Small back dots on the fault surface are locations of asperities. Top of the fault segment at top Souvré to bottom model, including the entire height of the Dinantian carbonate reservoir and part of the Devonian. White line indicates top Pont d'Arcole. The black plane shown intersecting fault EW-1 correponds to fault NS-1. Note that x- and y-coordinates in a) and b) are model coordinates (mesh rotated 17.5° anticlockwise for optimalisation).

segments of EW-1 follow the Mohr–Coulomb criterion with μ= 0.63, C_0 = 0 MPa and no weakening, representing aseismic slip behavior. Given the fault orientation and assumed frictional properties, initial stress conditions are chosen such that the fault section within the Dinantian carbonates and Devonian sandstones is reactivated at a pressure increase of just 0.3 MPa. An initially close-to-critically stressed fault is consistent with the early onset of seismicity observed after injection began.

No interfaces are included for faults NS-1 and EW-2, meaning these faults are locked and cannot slip. Consequently, fault–fault interaction is not considered in this model.

For the analysis of fault stability, we use both Coulomb stress and Coulomb stress change on fault EW-1, which is an important proxy for the seismicity potential of the fault. Coulomb stress (τ_{cs}) is defined as:

$$\boldsymbol{\tau_{cs} = \tau - \mu\sigma'_n = \tau - \mu\sigma_n - \mu P} \quad (2)$$

where τ is shear stress, σ_n is the total normal stress on the fault, σ'_n is the effective normal stress on the fault, μ is friction coefficient of the fault and P is the pore pressure on the fault. A zero or positive Coulomb stress means that fault strength is exceeded. A positive Coulomb stress *change* indicates that the stress on that fault segment follows a destabilizing path. The first two components on the right-hand side in both equations denote the contribution of changes in shear and normal stress due to poro- and thermoelastic stressing and stress transfer by aseismic slip; the component μP gives the contribution of the "direct pore pressure effect" in the fault. In our analysis we use the maximum value of the shear stress, i.e. we don't distinguish between the along-strike or dip-slip components of the shear stress.

We analyze the dynamic evolution of pressure, temperature and monitor the Coulomb stress and Coulomb stress changes that occurred on the fault EW-1 during the two operational phases. We investigate the contribution of the four mechanisms – pressure diffusion, poroelasticity, thermoelasticity and aseismic slip – to fault loading and subsequent fault reactivation over both temporal and spatial domains. In our analysis, we specifically focus on the loading of the asperities. The effects of direct pressure and poroelastic stress change on fault EW-1 can be determined by employing an elastic material model for the entire interface and assuming a zero thermal expansion coefficient. Modifying the thermal expansion coefficient to 1.e-5 allows us to investigate the additional stress contribution due to the cooling of surrounding rocks. The influence of aseismic fault slip and stress transfer onto the asperities can be determined by imposing a Mohr-Coulomb failure criterion (without weakening) on the interface, while maintaining the elastic behavior of asperities.

3.5. Parameter uncertainties and sensitivity analysis

Because of the limited availability of site-specific input data, a sensitivity analysis has been conducted to evaluate the impact of parameter uncertainty on the model results. Given the high computational cost of the three-dimensional numerical simulations, the sensitivity analysis was restricted to a limited set of key parameters. The sensitivity analysis was performed relative to the base-case model by varying one parameter at a time, while all other parameters were held constant (Table 2). This approach allows to assess the isolated effect of individual parameters on the model behaviour.

Table 2
Sensitivity scenarios and parameter variation.

Scenario	Parameter	Variation	Basecase
1[a]	Young's modulus (GPa)	E_{min}: 20	40
1[b]		E_{max}: 60	
2[a]	Biot coefficient (-)	α_{min}: 0.3	0.6
2[b]		α_{max}: 1.0	
3[a]	Thermal expansion coefficient (/°C)	$\alpha_{th,min}$: 0.2e-6	1.0e-5
3[b]		$\alpha_{th,max}$: 5.0e-5	
4[a]	Fault permeability // (m^2) (EW-1-NS-1)	k_{min} //: basecase*0.1	See Table 1
4[b]		k_{max} //: basecase*10	
4[c]	Fault permeability ⊥ (m^2) (EW)	k_{max} ⊥: 5.0e-16	1.0e-16
5[a]	Fault porosity (-)	n_{min}: basecase*0.5	NS-1 0.05, EW-1 0.025
5[b]		n_{max}: basecase*4	
5[c]	Matrix and fault porosity (-)	n_{max}: base case*4	See Table 1
6	Fault width	2.5,5 (EW-1,NS-1)	10,20 (EW-1,NS-1)
7	Criticality (MPa)	1.0	0.3
8	Friction coefficient asperity (-)	0.70	0.65

4. Modelling results

4.1. Pressure and temperature evolution

Fig. 6 shows the lateral distribution of pore pressure and temperature changes in the reservoir and the pore pressure changes on the fault EW-1 at the end of phase II. The pore pressure changes on fault EW-1 reach slightly above 2 MPa in the upper part of the fault close to the injection well, decreasing with depth and distance from the injection well. The temperature changes are limited to the near-well area and the thermal front itself does not reach fault EW-1.

4.2. Coulomb stress changes – contributions of direct pressure effect, poro- and thermoelasticity

Fig. 7a shows the total Coulomb stress changes on fault EW-1 at the end of phase II for an *elastic interface* (i.e. non-slipping interface). Fig. 7b to d present the individual contributions of the direct pressure effect (b), the poroelastic loading (c) and the thermoelastic loading (d). The direct pressure effect is clearly dominant over poroelastic and thermoelastic loading. Poroelastic stress changes tend to stabilize the shallower fault section to the West of the injection well, whereas they slightly destabilize the shallower eastern and deeper section of the fault (Fig. 7c). However, this poroelastic loading is limited, partially due to the assumption of a low coupling (α = 0.6) between deformation and stressing in the fractured carbonates. Fig. 7d demonstrates that, even though the thermal front itself does not reach the fault, some effects of thermal stresses are observed on the fault, when the thermal expansion is accounted for (α_{th} = 1.e-5 $°C^{-1}$). Shear and normal stress changes imposed by the thermal loading counteract the effect of the poroelastic loading (thermal contraction of rock versus poroelastic expansion during injection). The shallow fault segment close to the injection well is further destabilized due to the thermal stresses. Simulated thermal stresses are limited, due to the relatively short injection time and limited volume of injected cold fluids.

Fig. 8a shows the evolution of Coulomb stresses at asperity 1, located at the shallow fault segment west of the injection well (*elastic interface and* $\alpha_{th} = 0\ °C^{-1}$). Pressure diffusion dominates the stress development, but poroelastic loading adds a stabilizing effect during periods of injection by increasing total normal stress (clamping the fault) and reducing shear stress. Notably, the peak Coulomb stress changes in phase I at this fault segment occur just *after* the power-cut (after XI). This peak results from rapid poroelastic unloading due to a sudden reduction in flow rate, causing a quick contraction of the rock volume around the injection well.[27] The poroelastic unloading is faster than pressure release due to diffusion; while stabilizing effects of poroelasticity vanish rapidly after flow stops, pore pressure decreases more slowly, maintaining elevated fault pressure for some time. Similar poroelastic responses are seen at the end of each injection cycle in both phase I and phase II (not shown), briefly destabilizing the shallow fault segment west of the injection well after injection reductions. Although the

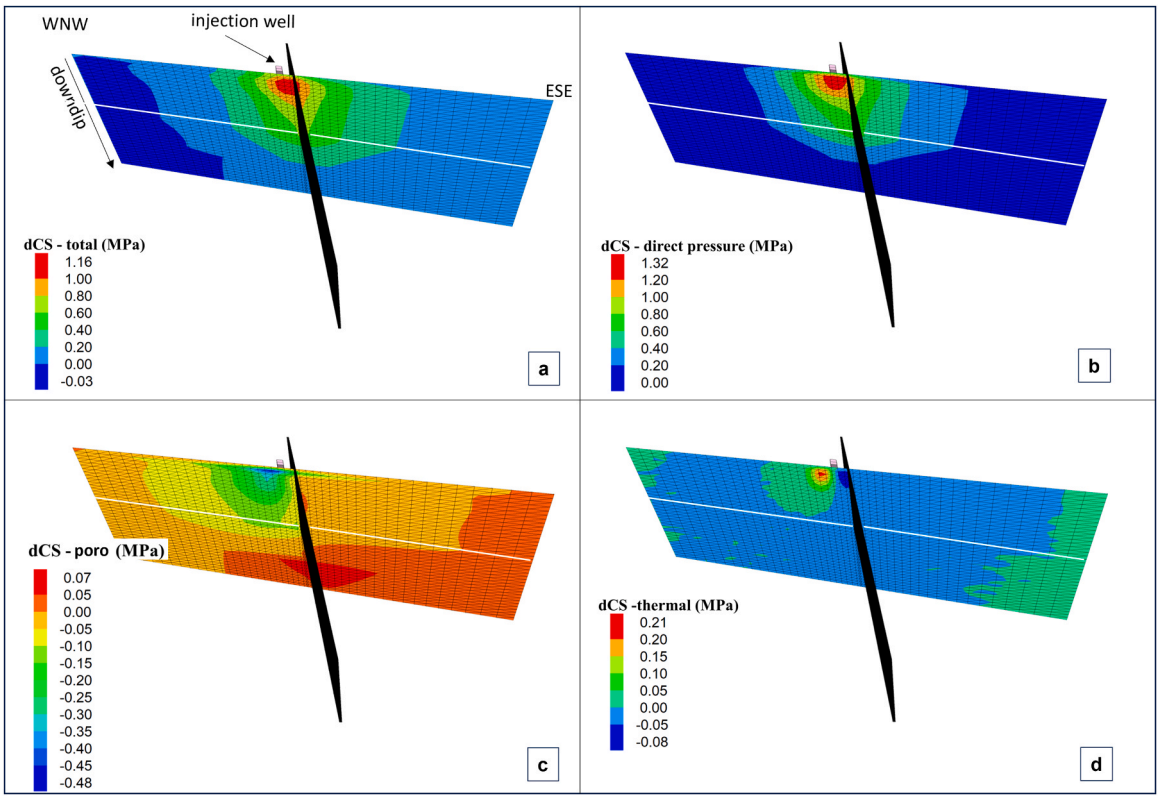

Fig. 7. a) Total Coulomb stress change at the time of the M 2.1 event, end of phase II at fault EW-1, b) Coulomb stress change due to direct pressure effect (*elastic interface)*, c) due to poroelastic effect (*elastic interface and* $\alpha_{th} = 0°C^{-1}$), d) due to thermal effect (*elastic interface and* $\alpha_{th} = 1.e\text{-}5°C^{-1}$). Note the different scales of the colorbar. Top of the fault segment at top Souvré (-3150 m) to bottom model (-5000 m), including the entire height of the Dinantian carbonate reservoir and part of the Devonian. White line indicates bottom Dinantian carbonates. The black plane shown intersecting fault EW-1 correponds to fault NS-1.

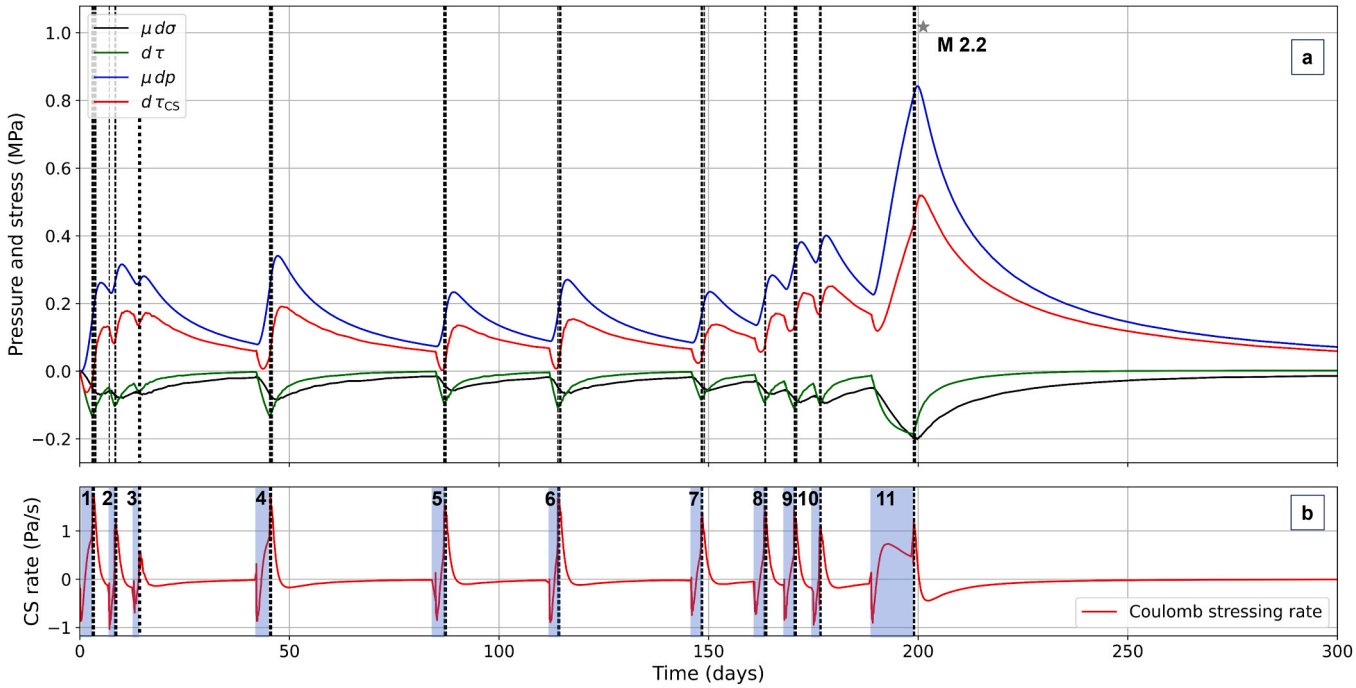

Fig. 8. Coulomb stress and stressing rates at location of asperity 1 (-3250 m depth) on fault EW-1, for *elastic interface and* $\alpha_{th} = 0\,°C^{-1}$) for phase I: a) Time-dependent Coulomb stress changes. Red line ($d\tau_{cs}$): total Coulomb stress change, blue line: direct pressure contribution (μdP), green line: shear stress contribution (dτ), black line: normal stress contribution (μdσ). b) Time-dependent Coulomb stressing rates. Black dashed vertical lines indicate time of maximum Coulomb stressing rates just after the end of each injection cycle. Grey-shaded areas represent injection intervals I-XI in well Mol-GT-02. Grey star depicts timing of M_L 2.2 seismic event. For location of asperity 1, see Fig. 6c. Coulomb stress (change) for asperities is computed based on μ= 0.65.

magnitude of the Coulomb stress peaks at the end of the injection cycles is low, the rates of positive Coulomb stress changes at the end of each cycle are relatively high, see Fig. 8b.

Fig. 9a and b illustrate the evolution of Coulomb stress throughout the injection and production phases for the asperity located beneath the injection well at an intermediate depth of 3800 m and 4200 m, assuming an elastic interface and a thermal expansion coefficient of $\alpha_{th} = 1 \times 10^{-5}$ $^{\circ}C^{-1}$.

In both asperities, the maximum Coulomb stress is reached at the end of the second prolonged injection cycle (II.10), approximately 1400 days after the start of injection.

A comparison of the individual components—direct pressure effect ($\mu\Delta P$), shear stress change ($\Delta\tau$), and normal stress change ($\mu\Delta\sigma$)—as shown in Figs. 7–9b, reveals that the magnitudes of Coulomb stress changes due to poro- and thermoelastic loading are small. These results confirm that pressure diffusion is the dominant mechanism driving Coulomb stress changes, outweighing the contributions from poroelastic and thermoelastic loading. Fault slip initiation is therefore primarily governed by pressure diffusion.

4.3. Coulomb stress changes – relative contributions of aseismic slip

Fig. 9c shows results for asperity 4, this time embedded in a frictional interface. Coulomb stress levels are significantly higher than in the elastic, no-slip case. Aseismic slip associated with three major slip events (initiating around days 200, 1100, and 1300) during extended injection periods transfers shear stress to the deeper asperity, substantially increasing its Coulomb stress.

Fig. 10a-e show the Coulomb stress evolution in time for the five asperities on the fault, comparing the two modelling cases: 1) with pore pressure diffusion, poroelasticity and thermoelasticity, and 2) also including aseismic slip on the fault surrounding the asperities, with accumulation of stresses on the asperities. The black dashed lines show the magnitude of the Coulomb stress (mark, not stress *change*) at the five asperities. Fault reactivation occurs if the Coulomb stress magnitude on the asperities exceeds 0. The graph also shows the combined contribution of the mechanisms of pressure diffusion and poro- and thermoelastic loading to fault Coulomb stress *changes* (green shaded area). Additionally, the Coulomb stress *change* which is entirely due to

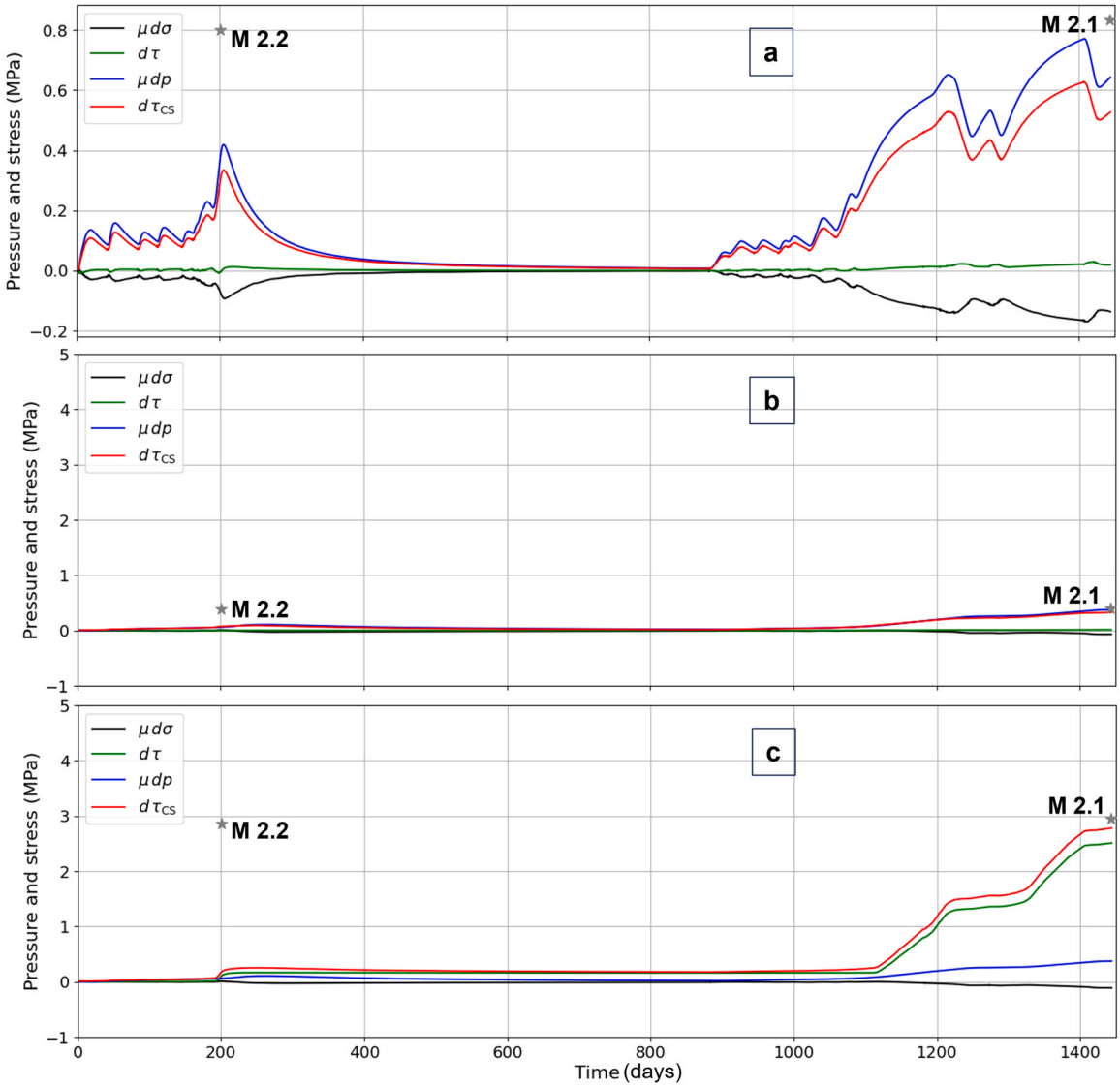

Fig. 9. a) Time-dependent Coulomb stress changes at the location of asperity 3 (-3800 m depth) on fault EW-1, for *elastic interface, with* α_{th} *= 1.e-5* $^{\circ}C^{-1}$, b) Time-dependent Coulomb stress changes at location of asperity 4 (-4200 m depth) on fault EW-1, for *elastic interface, with* α_{th} *= 1.e-5* $^{\circ}C^{-1}$, c) Time-dependent Coulomb stress changes at location of asperity 4 (-4200 m depth) on fault EW-1, for *frictional interface with aseismic slip and* α_{th} *= 1.e-5* $^{\circ}C^{-1}$. Red line ($d\tau_{cs}$): total Coulomb stress change, blue line: direct pressure contribution (μdP), green line: shear stress contribution $d\tau$, black line: normal stress contribution ($\mu d\sigma$). For the location of asperities, see Fig. 6c. Note that Coulomb stress (change) for asperities is computed based on μ= 0.65.

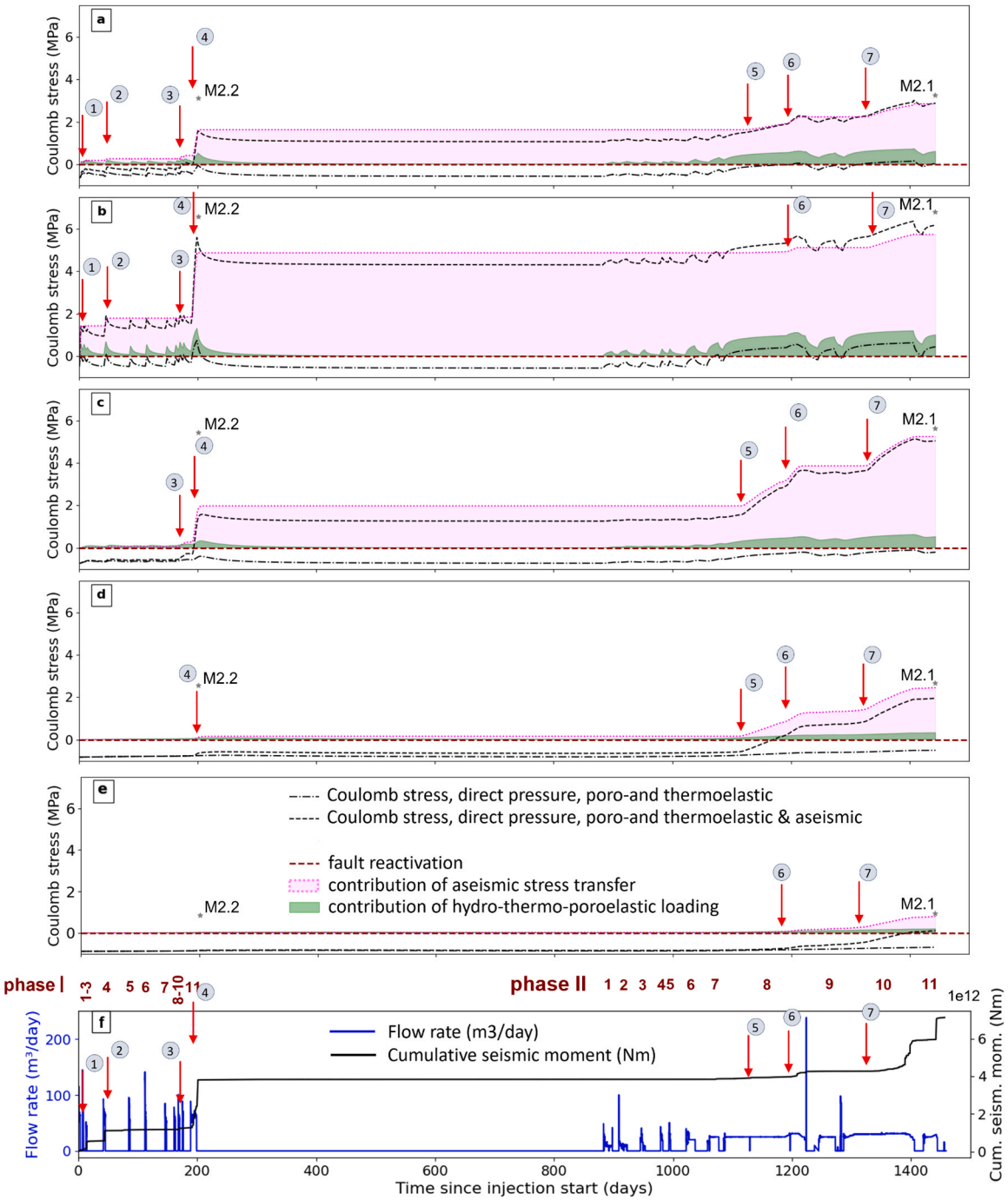

Fig. 10. Contribution of 'aseismic' slip to loading of the asperities, compared to contributions of other mechanisms, at different locations at increasing distance from the injection well. a) location 1, to the west of the injection well, depth −3250 m, b) location 2, to the east of the injection well, depth −3250 m, c) location 3, below the injection well, depth −3800 m, d) location 4, at a depth of ~4200 m, e) location 5, at a depth of ~4400 m, f) observed cumulative seismic moment release and measured flow rates. Dark red dashed line indicates Coulomb stress (CS) = 0; fault reactivation will occur at CS > 0. Green shaded area indicates cumulative Coulomb stress change caused by mechanisms of direct pressure change, poro- and thermoelasticity. Pink area bounded by magenta dashed line indicates Coulomb stress change entirely due to aseismic stress transfer. Black dashed lines show resulting magnitudes of Coulomb stress. Red arrows indicate the start of seven periods of aseismic fault reactivation. Coulomb stress (change) for asperities is computed based on μ= 0.65.

simulated aseismic fault slip and associated stress transfer onto the asperities is shown (magenta shaded area).

Sudden, permanent increases in Coulomb stress on the asperities correspond to stress transfer associated with aseismic slip on the fault. Seven main periods of aseismic fault slip can be observed, transferring stress to the asperities. The start of the aseismic slip periods is indicated by small red arrows in Fig. 10a-e. We observe a relatively small slip event almost directly after the start of injection (cycles I.1–3, with stress transfer to asperities 1–2), during cycle I.4 (asperities 1–2), and cycle I.8–10 (asperities 1–3). A major slip event is induced during the last injection cycle of phase I, which affects the asperities (1−4) on the shallow and intermediate sections of the fault. The deeper fault Section is not affected by this major slip event. Three additional slip events occur during periods of prolonged injection in phase II.8 and II.10, with largest Coulomb stress increase occurring on asperities 3,4 and 5. Fig. 11 shows the propagation of the pressure-induced aseismic-slip front in time, with

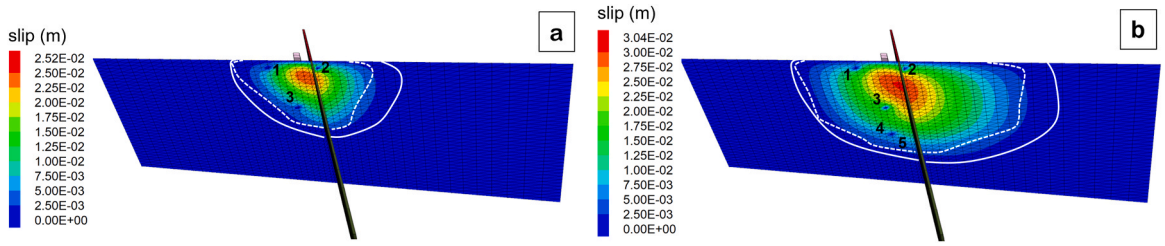

Fig. 11. a) Evolution of slip displacement due to aseismic slip on the fault EW-1, at the time of M_L 2.2 (end phase I) and b) M_L 2.1 event (end phase II). Numbers indicate locations of simulated asperities on the fault. White solid line presents extension of aseismic slip front. White dashed line presents dP = 0.3 MPa contour. The black plane shown intersecting fault EW-1 corresponds to fault NS-1.

the aseismic-slip front ahead of the pressure front (here defined as dP = 0.3 MPa, based on the criticality of the fault). A vertical profile through the deeper asperities (Fig. 12) shows pore pressure changes, relaxation of shear and normal stress behind the aseismic front, and the loading of the asperities by transfer of the shear stress.

Building on the observations from Figs. 7 to 9a, which revealed that pressure change plays a larger role in fault loading than poroelastic and thermoelastic loading, Fig. 10 further suggests that already soon after the start of the injection, pressure diffusion induces aseismic fault slip at shallow and intermediate fault sections near the injection well. During later stages of phase I and phase II, the aseismic stress transfer is the dominant loading mechanism of the asperities, particularly in the deeper fault segments.

4.4. Parameter uncertainties and sensitivity analysis

Input parameters, such as rock permeability, porosity and poroelastic properties affect pressure, temperature and stress changes within the reservoir. In combination with the criticality of the aseismic fault segment and the strength of the asperities, these parameters affect Coulomb stress changes and the potential for seismic slip on the asperities. Results of the sensitivity analysis show the temporal and spatial evolution of the Coulomb stress changes on the asperities depending on the parametrisation.

A clear sensitivity of pore pressure, Coulomb stress and slip to Young's modulus (1a,b) and Biot's coefficient (2a,b) is observed (Figs. 13 and 14). A higher Young's modulus results in larger Coulomb stress changes and vice versa. A reverse trend is observed for the Biot coefficient. This sensitivity of pore pressure, slip and Coulomb stress to the Biot coefficient and Young's modulus of the matrix and fault damage zone is largely linked to changes in pore pressure diffusivity (Fig. 13a and b), rather than poroelastic changes of the total normal and shear stress. Diffusivity (D) in a poroelastic medium depends on porosity, permeability, Biot coefficient, elastic parameters bulk and shear modulus (K,G), fluid modulus (K_f) and fluid viscosity (μ_{visc}):

$$\boldsymbol{D} = \frac{\boldsymbol{k}}{\boldsymbol{\mu_{visc}}} \bullet \left(\frac{\mathbf{1}}{\boldsymbol{M}} + \frac{\boldsymbol{\alpha^2}}{\boldsymbol{K} + \frac{4\boldsymbol{G}}{3}} \right)^{-1} \tag{3}$$

with Biot modulus: $M = K_f/n + (\alpha - n)(1 - \alpha)\left(\frac{K_f}{K}\right)$. The effect of diffusivity on pore pressure and Coulomb stress change is also clear in the scenario with high porosity for the entire rock mass (5c), but is smaller for changes in fault porosity only (5a,b).

Coulomb stress changes are less sensitive to variations in the thermal expansion coefficient (3a,b); variations affect only the two upper asperities (Fig. 14). The sensitivity to along-fault permeability (4a,b)

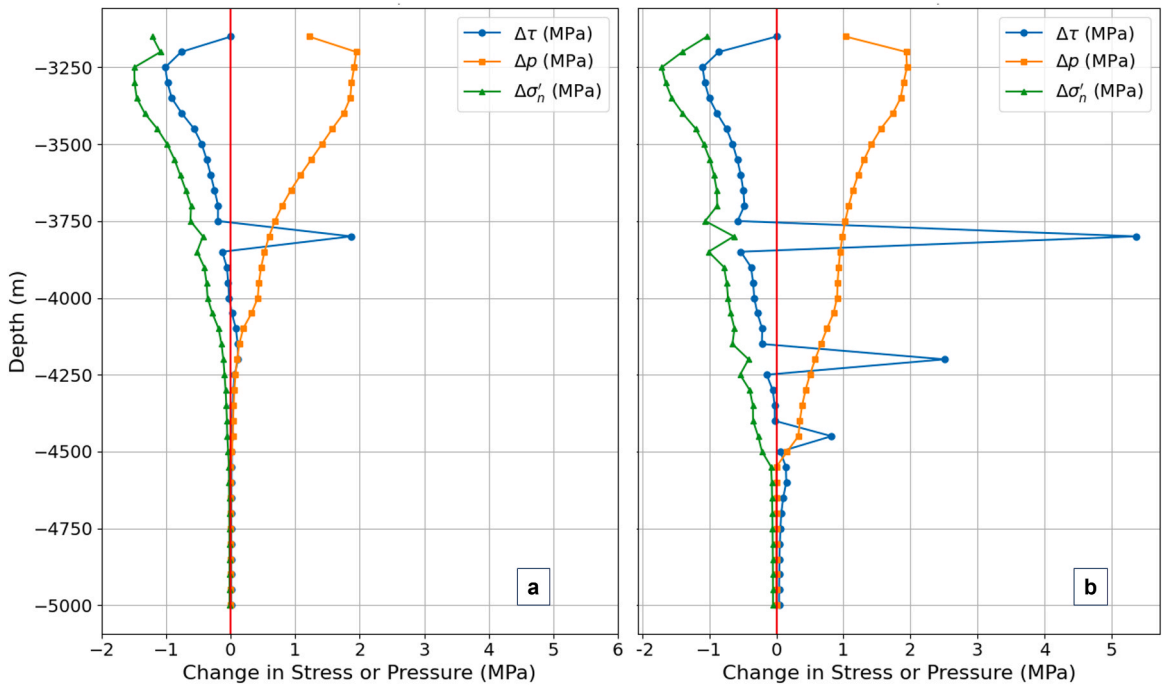

Fig. 12. Pressure and stress change on fault EW-1, along a vertical line through the asperities 3, 4 and 5; a) at the time of the M_L 2.2 event, phase I and b) at the time of the M_L 2.1 event, phase II. ΔP, $\Delta\sigma_n$' and $\Delta\tau$ is pressure, effective normal stress and shear stress change, respectively.

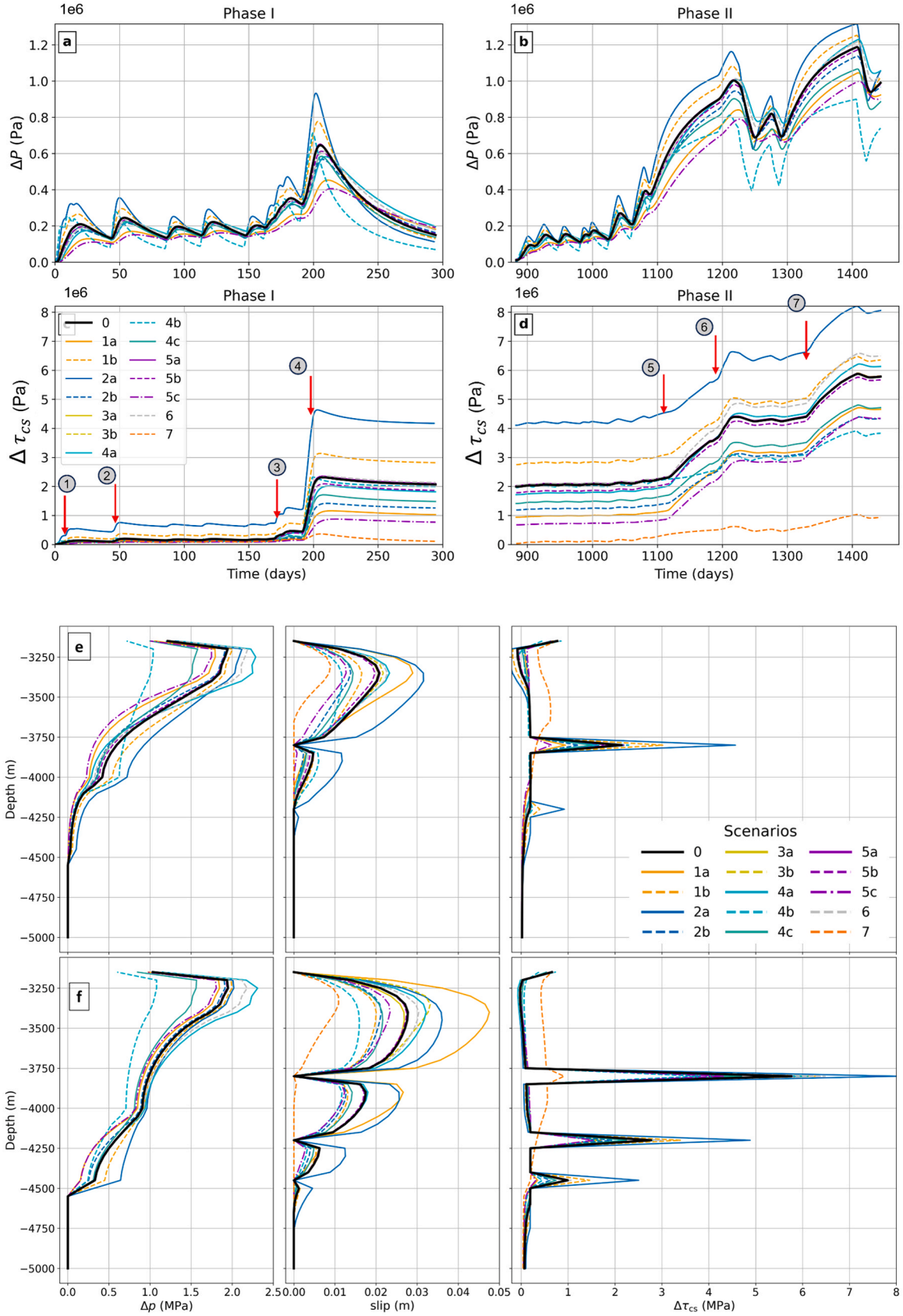

Fig. 13. Pressure and stress change versus time on asperity 3 (-3800 m depth) for different sensitivity scenario's, a) pressure change during phase I, b) pressure change during phase II, c) Coulomb stress change (incremental from start phase I) during phase I, d) Coulomb stress change (incremental from start phase II) during phase II, e) pressure change, slip and Coulomb stress change on a vertical profile through asperities 3–5, phase I and f) phase II.

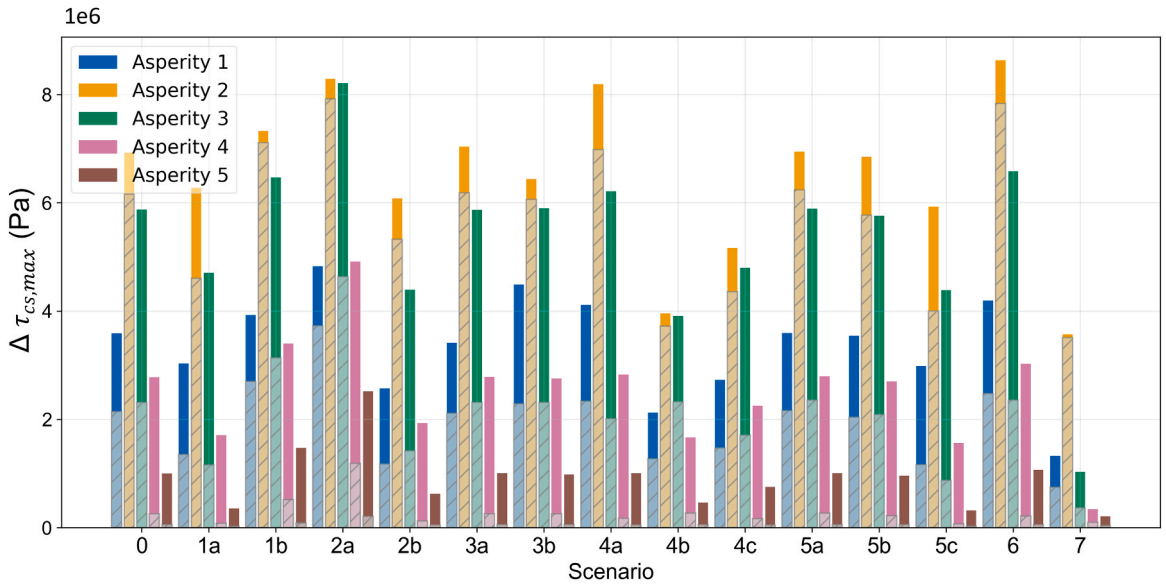

Fig. 14. Results of sensitivity analysis: maximum Coulomb stress change ($\Delta\tau_{cs,\max}$) for phase I (grey-shaded) and phase II (colored), for all sensitivity scenarios.

depends on the location of the asperities and the operational phase. Changes in along-fault permeability influence both fault diffusivity and transmissivity. Low along-fault permeability leads to steep pressure gradients, concentrating pressure changes near the well and at shallow depths. In contrast, high along-fault permeability promotes less steep pressure gradients and pressure diffusion to greater depths, resulting in larger pressure changes and Coulomb stressing on the deeper asperities in phase I (Fig. 13e), where diffusion rates are more important due to high injection rates, short cycles causing stronger transients than in phase II. A lower across-fault permeability in fault EW-1 (4c) lowers the resistance to flow in the NS-1-fault – thereby significantly decreasing the Coulomb stress that builds up on fault EW-1 (Fig. 14). A reduction of fault damage zone width (6) reduces transmissivity and storage, resulting in higher Coulomb stresses on fault EW-1. Low fault criticality of the aseismic segment (7) delays and reduces aseismic slip events, transferring less stress to the asperities (Figs. 13f and 14). A higher friction coefficient for asperities (8) has limited effect on Coulomb stress change, but decreases Coulomb stress magnitude (not shown here), and thus delays asperity reactivation.

The sensitivity analysis reveals consistent patterns in both the number and timing of the main aseismic slip events, similar to those observed in the base case model. Sudden, permanent increases in Coulomb stress on the asperities correspond to stress transfer associated with aseismic slip on the fault (Fig. 13c and d, indicated by red arrows). In all scenarios, asperities nearest the injection well (1−2) are predominantly loaded during operational phase I, whereas loading of the deeper asperities becomes more pronounced during operational phase II (Fig. 14).

While absolute magnitudes of Coulomb stress changes vary across scenarios, all but scenario 7 reproduce trends similar to the base case model regarding the dominant contribution of fluid pressure-induced aseismic slip and stress transfer, as well as the timing of aseismic slip events. In scenario 7 with lower fault criticality, aseismic slip occurs only locally near the injection well, and does not significantly affect the asperities at larger depth (Fig. 13e and f).

5. Discussion

Our model results indicate that thermoelastic effects remain relatively small, and are limited to the area closest to the injection well. This is due to the limited injected fluid volumes, but effects may increase with prolonged injection. We note that the single-porosity approach adopted here may not fully capture the thermal and stress response of a fractured medium, where flow is fracture-dominated and the matrix controls storage and cooling. In such settings, cold water propagates rapidly through fractures, generating a diffuse thermal front, controlled by matrix–fracture interactions and fracture density.[28] In our simulations, the single-porosity approach produces a sharp temperature front. This may overestimate cooling near the injection well (close to fault EW-1) and underestimate thermal effects at larger distances, particularly in the case of a large fracture spacing. However, given the relatively short injection periods and small injected volumes, this effect is expected to be limited compared to pressure-driven and aseismic-slip effects, particularly at greater distances and depths.

Comparison with main characteristics of seismicity. In terms of timing, the simulated aseismic slip episodes correlate well with periods of significant seismic moment release and increased seismic activity (Fig. 10). In both modelling results and observations, four distinct aseismic slip events can be identified during Phase I, separated by intervals of limited stress transfer and negligible aseismic slip. Specifically, aseismic slip occurs shortly after the start of injection during cycles I.1–I.3, followed by a slip episode in Phase I.4. This is succeeded by a quiescent period between Phases I.4 and I.8, after which renewed aseismic slip and associated stress transfer occur during Phases I.8–I.10. A final, dominant slip event is induced in Phase I.11, coinciding with the sharp increase in seismic moment release associated to the M_L 2.2 event recorded just after shut-in of cycle I.11. A similar correspondence between the timing of simulated aseismic slip and stress transfer to asperities and the observed increases in seismic activity and seismic moment release is observed during Phase II. Two main aseismic slip events are simulated during Phase II.8, the second of which coincides with the increase in injection flow rate at the end of this cycle. This is followed by a quiescent interval during Phase II.9, characterized by limited stress transfer and low seismic moment release. Seismic slip and stress transfer resume during the second half of Phase II.10, aligning with a renewed increase in observed seismicity rate and seismic moment release. We note that the model does not predict significant aseismic slip during the earlier stages of Phase II, whereas observations indicate the early occurrence of microseismic events detected by the deep sensor.

A quantitative comparison between the simulated spatial distribution of stress changes and the locations of observed events is challenging due to uncertainties in seismic event hypocenters (particularly for Phase I), limited knowledge of fault geometry from sparse 2D seismic lines, and the simplified model geometry with focus on the single fault near the

injection well. Nevertheless, Figs. 10 and 14 show stress transfer progressing to greater depths over time, consistent with observations. Asperities closest to the injection well (1–3; ≥ –3800 m depth) are predominantly loaded during operational Phase I, whereas the first loading of the deepest asperity 5 (–4400 m depth) occurs in the second half of Cycle II.10, in line with the sudden occurrence of deep seismic events in the observations at the end of Cycle II.10.

Assumption of aseismic fault section with isolated asperities. In our geomechanical model, we assume that the WNW-ESE fault, that hosts the majority of the seismic events close to the injection well, is characterized by a few isolated asperities located far apart. The area surrounding these asperities is assumed to slip aseismically, without a significant stress drop. Another end-member would be a fault which is fully covered by seismic asperities, where fault slip is mainly accommodated by repeated seismic events and stress transfer between asperities governs the evolution of seismicity, and aseismic slip plays no role. The validity of our assumption can be tested against the concept of effective stress drop as introduced by Fisher and Hainzl[29] for seismic swarms – a swarm being a sequence of earthquakes, such as the observed seismic cloud, that occur in a localized area over a relatively short period of time, without a single clearly dominant mainshock or foreshock-aftershock sequence. The effective stress drop $d\sigma_e$ of a seismic swarm is defined as:[29]

$$d\sigma_e = \frac{7M_{0,seismic}}{16R^3} \tag{4}$$

Where $M_{0,seismic}$ is the cumulative seismic moment during the swarm and R is the radius of the seismicity area, assuming it is circular to first order. Effective stress drops for seismic swarms that are in the range of earthquake stress drops (1–100 MPa) suggest that the slipping area is mostly covered by seismic asperities; low effective stress drops for seismic swarms on the other hand suggest that seismic asperities are far apart, and have been proposed to indicate a large contribution of aseismic slip to fault movement.[12,29]

Applying the concept of effective stress drop for the seismic cloud of the Mol geothermal site, we derive a R of approximately 500 m for phase II, under the assumption that all seismicity occurred on the WNW-ESE fault close to the injection well – see Fig. 4b for the seismicity cloud projected onto the EW-1 fault. Using the site-specific relation between local and moment magnitude for the Mol geothermal site,[20] we compute a cumulative seismic moment release of $\sim 7 \times 10^{12}$ N.m in the period 2018 to end 2022.

$$M_w = 0.7M_L + 0.52 \tag{5}$$

$$M_{0,seismic} = 10^{1.5(M_w+6.033)} \tag{6}$$

From Eq. 4 we then obtain an upper bound for the effective stress drop of 0.025 MPa. This low value supports our hypothesis of an aseismically slipping fault with a few isolated asperities.

Additional evidence for the reactivation of isolated asperities comes from the observation that the majority of seismic events close to the injection well consists of multiplets and seismic repeaters, and from the occurrence of isolated 'families' of events as interpreted in the seismic data.[6] Additional constraints from fault zone structure and seismic source scaling parameters would further strengthen this interpretation. Such information may become available in the future through detailed seismological analyses of the events and improved characterization of fault geometry from 3D seismic data. However, these data were not available at the time of writing, and a comprehensive seismological analysis lies beyond the scope of the present study.

Seismic versus aseismic slip on asperities. In the current model, the asperities are elastic, and aseismic slip is imposed by assigning frictional behaviour without weakening and dilation to the surrounding fault surface. This simplified approach provides insight into the cumulative loading of the asperities via stress transfer by aseismic slip, but it does not account for slip on the asperities itself, and the stability of this slip (i.e. seismic or aseismic). Friction experiments demonstrate that frictional resistance evolves during sliding and is influenced by factors such as slip rate, magnitudes and changes of effective normal stress, temperature, mineralogy, grainsize and fault gouge structure. The stability of fault slip depends on this evolution of frictional resistance during sliding.[30–36] An analysis of fault friction evolution and slip stability falls outside the scope of this study. However, we note that there may be a competition between stress magnitude and stressing rate in controlling seismic fault slip, which could be relevant for the Mol geothermal site. Based on rate-and-state friction theory, studies[37,38] show that under steady injection, stress magnitude dominates, promoting either seismic or aseismic slip depending on whether effective normal stress is high or low, respectively. In contrast, the stressing rate can become critical during sudden changes in flow. Although elevated seismic activity was mainly observed during periods of relatively prolonged injection (e.g. at the end of the last and longest injection period of phase I (I.11) and after extended injection in the last cycles of phase II (Fig. 3), seismic events were also recorded during and after shut-in.[6] High stressing rates are modeled immediately after the end of injection cycles, attributed to poroelastic effects linked to rapid reductions in flow rate and pressure (Fig. 8). Although increasing seismic activity prior to the accidental power cut suggests fault reactivation had already begun before shut-in, high Coulomb stressing rates due to poroelastic unloading immediately after the shut-in may have contributed to the occurrence of the main M_L 2.2 event. Some smaller seismic events were reported during shut-in phases, further indicating that stressing rate effects may have influenced fault slip behaviour. Additionally, the increase in effective normal stress resulting from reduced fault pressure following shut-in may have facilitated seismogenic slip.[6,37,38]

Several recent studies have highlighted the role of fluid-induced aseismic slip based on field observations, modelling studies, and laboratory experiments.[11–17,26,27,39] Consistent with these findings our simulation results indicate that aseismic stress transfer, driven by elevated fluid pressures and to a lesser extent thermo-poroelastic loading near the injection well, can also play a key role in fault stressing and reactivation at the geothermal site in Mol. Assuming a near-critical initial stress, this aseismic slip propagates ahead of the pressure front, which we define in this context as the pressure change corresponding to the criticality of the fault. The aseismic slip transfers stress to fault asperities located farther from the injection well at progressively greater depths.

Relevance for operational strategies and mitigation. Differences in operational protocols—such as short-duration, high-rate injection and production versus longer-duration, low-rate injection and production with equivalent injected volumes—can lead to distinct patterns of pore-pressure build-up and dissipation, aseismic slip, and stress accumulation and release. These differences are likely to influence both the total seismic moment release and the event-size distribution. At the Mol geothermal site, a traffic light system is implemented to mitigate induced seismicity. Flow rates are reduced or wells are shut in when predefined thresholds are exceeded. For such mitigation strategies to be effective, intermittent no-flow periods must be sufficiently long to allow pore pressures to dissipate, not only near the injection well but also at larger distances and greater depths. This is particularly important because the increase in effective normal stress with depth promotes seismic responses at depth, as pore-pressure and aseismic slip fronts propagate downward during prolonged injection. For example, from Fig. 10d and e, we observe no significant pressure decrease at greater depths (asperity 4 and 5) during the no-flow period at the end of Phase II, which preceded the M_L 2.1 event.

Our simulation results suggest that, in addition to pore-pressure dissipation, relaxation of shear stresses accumulated at asperities during no-flow periods may be an important controlling factor in mitigating induced seismicity. Furthermore, diminishing rate effects associated with rapid changes in flow rate, related pore pressure changes and/or

poroelastic unloading may further reduce induced seismicity. In the current model, asperities are represented as elastic, resulting in a cumulative build-up of shear stress due to stress transfer from the surrounding aseismically slipping fault surface. Assessing the effectiveness of different operational strategies would require the implementation of more advanced friction laws for asperities, such as rate-and-state friction models[30–34] or the microphysical CNS model.[35,36] Such formulations would enable the simulation of asperity behavior in terms of stable and unstable slip, nucleation, stress drop, and stress relaxation between loading cycles, and support the optimization of operations. These effects have not been considered in the present study but will be addressed in future work.

The current model of the Mol geothermal site is simple and based on a limited dataset, including 2D seismic lines, well logs, and borehole descriptions, and also alignment of seismicity and focal mechanisms are used to define the geological framework. Due to the complex faulted and fractured geological structure and the limited amount of data, there are uncertainties associated with the geological framework and the parametrization of the model. Despite these uncertainties and the fact that the model geometry is simplified, and flow and mechanical behaviour are not fully constrained, the model has shown potential to reproduce important field observations of seismicity at the Mol geothermal site. The general trends and observations from the simulations provide valuable insights into the mechanisms contributing to seismicity at the Mol geothermal site and their relative impacts.

6. Conclusions

We have developed a geometrically simplified coupled model of the Mol geothermal site to simulate pressure, temperature and stress changes on a fault near the injection well. The fault was characterized by an aseismic fault surface and a few embedded asperities.

We performed a sensitivity analysis to explore the effects of uncertainty in model parameters. Though absolute magnitudes of Coulomb stress changes vary between scenarios, the analysis shows similar trends with regard to the dominant contribution of pressure and stress transfer due to aseismic slip, as well as to the timing of aseismic slip events and the progressive reactivation of deeper asperities with prolonged injection. The latter are consistent with the main characteristics of observed seismicity.

Thermal effects have had a limited influence on fault stress, particularly at the deeper asperities. This is primarily due to the relatively small injected volumes. Simulation results further suggest that stressing rate effects are important. Rapid poroelastic unloading immediately after shut-in and a later increase in effective normal stress due to declining fault pressure may have facilitated seismogenic slip after shut-in. Both mechanisms could have contributed to the induced seismicity observed post shut-in, including the M_L 2.2 event.

Aseismic slip, primarily driven by pressure increases, appears to have played a significant role in fault reactivation at the Mol geothermal site. The model results suggest that stress transfer from aseismic slip to fault asperities may have been a key driver of seismicity, particularly for larger events at greater depths and farther from the injection well. These findings indicate that, in addition to pore-pressure dissipation, the build-up and relaxation of shear stresses accumulated at asperities during flow and no-flow periods is an important factor to be considered in mitigating induced seismicity. Moreover, diminishing rate effects associated with rapid changes in flow rate, pore-pressure variations, and/or poroelastic unloading may further reduce seismicity.

Aseismic slip is inherently difficult to detect, therefore it presents a challenge for seismic hazard assessment and mitigation. It is thus essential to complement seismic monitoring with techniques capable of detecting aseismic fault movements. This will enhance our understanding of fault behavior and improve risk mitigation strategies - not only for the Mol geothermal site but also for other geothermal project within the Dinantian carbonates and similar geological formations.

CRediT authorship contribution statement

Loes Buijze: Writing – review & editing. **Matsen Broothaers:** Writing – review & editing, Methodology. **de Bresser Hans:** Writing – review & editing. **Justin Pogacnik:** Writing – review & editing, Methodology. **Wassing Brecht:** Writing – original draft, Methodology, Formal analysis, Conceptualization.

Declaration of Competing Interest

The authors declare that they have no known competing financial interests or personal relationships that could have appeared to influence the work reported in this paper.

Acknowledgements

During the preparation of this work the author(s) used Copilot in order to improve language and readability. After using this tool/service, the author(s) reviewed and edited the content as needed and take(s) full responsibility for the content of the publication.

Data availability

Data will be made available on request.

References

1. Buijze L, van Bijsterveldt L, Cremer H, et al. Review of induced seismicity in geothermal systems worldwide and implications for geothermal systems in the Netherlands. *Neth J Geosci.* 2019;98, e13. https://doi.org/10.1017/njg.2019.6.
2. Bos S, Laenen B. Development of the first deep geothermal doublet in the Campine Basin of Belgium. *Eur Geol.* 2017;43:16–20.
3. Broothaers M, Bos S, Lagrou D, Harcouët-Menou V, Laenen B. Lower carboniferous limestone reservoir in northern Belgium: structural insights from the Balmatt project in. *Mol Proc Eur Geotherm Congr.* 2019 (Den Haag, The Netherlands).
4. Broothaers M, Lagrou D, Laenen B, Harcouët-Menou V, Vos D. Deep geothermal energy in the Lower Carboniferous carbonates of the Campine Basin, northern Belgium: An overview from the 1950's to 2020. *Z Dtsch Ges Geowiss.* 2021;172(3): 211–225. https://doi.org/10.1127/zdgg/2021/0285.
5. Broothaers M, Cox K, Harcouët-Menou V, et al. Status of the VITO geothermal project in the Carboniferous Limestone Group in the Belgian Campine Basin (Mol-Dessel area). *Proc Eur Geotherm Congr.* 2025 (Zurich, Switzerland).
6. Kinscher JL, Broothaers M, Schmittbuhl J, de Santis F, Laenen B, Klein E. First insights to the seismic response of the fractured Carboniferous limestone reservoir at the Balmatt geothermal doublet (Belgium). *Geothermics.* 2023;107, 102585. https://doi.org/10.1016/j.geothermics.2022.102585.
7. Pogacnik J, Hernandez E, Rombaut B, et al. VITO geothermal project (Mol, Belgium): reservoir conceptual and numerical model update. *Proc Eur Geotherm Congr.* 2025 (Zurich, Switzerland).
8. Boyet A, De Simone S, Ge S, et al. Poroelastic stress relaxation, slip stress transfer and friction weakening controlled post-injection seismicity at the Basel Enhanced Geothermal System. *Commun Earth Environ.* 2023;4:104. https://doi.org/10.1038/s43247-023-00764-y.
9. Vörös R, Baisch S. Induced seismicity and seismic risk management – a showcase from the Californië geothermal field (the Netherlands). *Neth J Geosci.* 2022;101, e15. https://doi.org/10.1017/njg.2022.12.
10. Hager BH, Dieterich J, Frohlich C, et al. A process-based approach to understanding and managing triggered seismicity. *Nature.* 2021;595:684–689. https://doi.org/10.1038/s41586-021-03668-z.
11. Bhattacharya P, Viesca RC. Fluid-induced aseismic fault slip outpaces pore-fluid migration. *Science.* 2019;364:464–468. https://doi.org/10.1126/science.aaw735.
12. Danré P, De Barros L, Cappa F, Ampuero JP. Prevalence of aseismic slip linking fluid injection to natural and anthropogenic seismic swarms. *J Geophys Res Solid Earth.* 2022;127, e2022JB025571. https://doi.org/10.1029/2022JB025571.
13. Duboeuf L, De Barros L, Cappa F, Guglielmi Y, Deschamps A, Seguy S. Aseismic motions drive a sparse seismicity during fluid injections into a fractured zone in a carbonate reservoir. *J Geophys Res Solid Earth.* 2017;122:8285–8304. https://doi.org/10.1002/2017JB014535.
14. Ciardo F, Lecampion B. Injection-induced aseismic slip in tight fractured rocks. *Rock Mech Rock Eng.* 2023;56:7027–7048. https://doi.org/10.1007/s00603-023-03249-8.
15. Lengliné O, Maurer V, Yorillo A. Intermittent induced seismicity during the multiyear operation of a geothermal reservoir. *Geophys J Int.* 2025;242(1), ggaf160. https://doi.org/10.1093/gji/ggaf160.
16. Wynants-Morel N, Cappa F, De Barros L, Ampuero J-P. Stress perturbation from aseismic slip drives the seismic front during fluid injection in a permeable fault. *J Geophy S Res Solid Earth.* 2020;125, e2019JB019179. https://doi.org/10.1029/2019JB019179.

17. Yang Y, Yang H, Zi J. Stress transfer outpaces injection-induced aseismic slip and triggers seismicity. *Sci Rep*. 2023;13, 16626. https://doi.org/10.1038/s41598-023-43760-0.
18. Heidbach O, Rajabi M, Di Giacomo D, et al. *World Stress Map Database Release 2025*. GFZ Data Services; 2025. https://doi.org/10.5880/WSM.2025.001.
19. Vanneste K, Camelbeeck T, Verbeeck K, Demoulin A. Morphotectonics and past large earthquakes in eastern Belgium. In: Demoulin A, ed. *Landscapes and Landforms of Belgium and Luxembourg*. Cham: Springer International Publishing; 2018 Chapter 13. doi:10.1007/978-3-319-58239-9_13.
20. Gautam R, Kinscher JL, Schmittbuhl J, Broothaers M, Laenen B. Contribution of a 2052m Deep Borehole Seismometer to Event Detection and Spatio-Temporal Characterization of Induced Seismicity at the VITO Geothermal Site. *Proc Eur Geotherm Congr*. 2025 (Zurich, Switzerland).
21. Gautam R., Kinscher J.L.,Schmittbuhl J., Broothaers M., and Laenen B. Contribution of a 2052m Deep Borehole Seismometer on characterisation of induced seismicity at Balmatt Geothermal site. Schatzalp 4th Induced Seismicity Workshop, Davos, Switzerland, 18-21 March, 2025.
22. Taron J, Elsworth D. Coupled Mechanical and Chemical Processes in Engineered Geothermal Reservoirs with Dynamic Permeability. *Int J Rock Mech Min Sci*. 2010; 47:1339–1348. https://doi.org/10.1016/j.ijrmms.2010.08.021.
23. Goense T. *Physical characterization of the Lower Carboniferous Limestone as a potential Geothermal Reservoir*. MSc thesis Delft Univ.Technol; 2018.
24. Soustelle V, ter Heege J, Wassing B. Relationship between static and dynamic elastic moduli in carbonates (Atlanta, GA, USA) *Proc 57th U S Rock Mech /Geomech Symp*. 2023 Jun. https://doi.org/10.56952/ARMA-2023-0331.
25. Kane E, Pluymakers A, Niemeijer A. Reactivation envelopes of immature and mature faults of Dinantian carbonates targeted for geothermal energy. Vienna, Austria; 24–28 Apr 2023 *EGU Gen Assem*. 2023. https://doi.org/10.5194/egusphere-egu23-11236.
26. Sáez A, Lecampion B. Post-injection aseismic slip as a mechanism for the delayed triggering of seismicity. *Proc R Soc A*. 2023;479, 20220810. https://doi.org/10.1098/rspa.2022.0810.
27. Segall P, Lu S. Injection-induced seismicity: Poroelastic and earthquake nucleation effects. *J Geophys Res Solid Earth*. 2015;120:5082–5103. https://doi.org/10.1002/2015jb012060.
28. Wassing BBT, Candela T, Osinga S, et al. Time-dependent seismic footprint of thermal loading for geothermal activities in fractured carbonate reservoirs. *Front Earth Sci*. 2021;9, 685841. https://doi.org/10.3389/feart.2021.685841.
29. Fischer T, Hainzl S. Effective stress drop of earthquake clusters. *Bull Seismol Soc Am*. 2017;107(5):2247–2257. https://doi.org/10.1785/0120170035.
30. Dieterich JH. Modeling of rock friction: 1. Experimental results and constitutive equations. *J Geophys Res*. 1979;84(B5):2161–2168.
31. Dieterich JH. Constitutive properties of faults with simulated gouge. *Pure Appl Geophys*. 1981;116:790–806.
32. Ruina A. Slip instability and state variable friction laws. *J Geophys Res*. 1983;88 (B12):10359–10370.
33. Rice JR, Tse ST. Dynamic motion of a single degree of freedom system following a rate and state dependent friction law. *J Geophys Res Solid Earth*. 1986;91:521–530.
34. Linker MF, Dieterich JH. Effects of variable normal stress on rock friction: Observations and constitutive equations. *J Geophys Res Solid Earth*. 1992;97(B4): 4923–4940. https://doi.org/10.1029/92JB00017.
35. Chen J, Spiers CJ. Rate and state frictional and healing behavior of carbonate fault gouge explained using microphysical model. *J Geophys Res Solid Earth*. 2016;121: 8642–8665. https://doi.org/10.1002/2016JB013470.
36. Chen J, Niemeijer AR. Seismogenic potential of a gouge-filled fault and the criterion for its slip stability: Constraints from a microphysical model. *J Geophys Res Solid Earth*. 2017;122:9658–9688. https://doi.org/10.1002/2017JB014228.
37. Alghannam M, Juanes R. Understanding rate effects in injection-induced earthquakes. *Nat Commun*. 2020;11:3053. https://doi.org/10.1038/s41467-020-16860-y.
38. Sun Z, Elsworth D, Cui G, Li Y, Zhu A, Chen T. Impacts of Rate of Change in Effective Stress and Inertial Effects on Fault Slip Behavior: New Insights Into Injection-Induced Earthquakes. *J Geophys Res Solid Earth*. 2024. https://doi.org/10.1029/2023JB027126.
39. Cebry SBL, Ke C-Y, McLaskey GC. The role of background stress state in fluid-induced aseismic slip and dynamic rupture on a 3-m laboratory fault. *J Geophys Res Solid Earth*. 2022;127, e2022JB024371. https://doi.org/10.1029/2022JB024371.